Publication Year	2017
Acceptance in OA@INAF	2021-02-23T08:30:05Z
Title	The size, shape, density and ring of the dwarf planet Haumea from a stellar occultation
Authors	Ortiz, J. L.; Santos-Sanz, P.; Sicardy, B.; Benedetti-Rossi, G.; Bérard, D.; et al.
DOI	10.1038/nature24051
Handle	http://hdl.handle.net/20.500.12386/30540
Journal	NATURE
Number	550

LETTER

doi:10.1038/nature24051

The size, shape, density and ring of the dwarf planet Haumea from a stellar occultation

J. L. Ortiz[1], P. Santos-Sanz[1], B. Sicardy[2], G. Benedetti-Rossi[3], D. Bérard[2], N. Morales[1], R. Duffard[1], F. Braga-Ribas[3,4], U. Hopp[5,6], C. Ries[5], V. Nascimbeni[7,8], F. Marzari[9], V. Granata[7,8], A. Pál[10], C. Kiss[10], T. Pribulla[11], R. Komžík[11], K. Hornoch[12], P. Pravec[12], P. Bacci[13], M. Maestripieri[13], L. Nerli[13], L. Mazzei[13], M. Bachini[14,15], F. Martinelli[15], G. Succi[14,15], F. Ciabattari[16], H. Mikuz[17], A. Carbognani[18], B. Gaehrken[19], S. Mottola[20], S. Hellmich[20], F. L. Rommel[4], E. Fernández-Valenzuela[1], A. Campo Bagatin[21,22], S. Cikota[23,24], A. Cikota[25], J. Lecacheux[2], R. Vieira-Martins[3,26,27,28], J. I. B. Camargo[3,27], M. Assafin[28], F. Colas[26], R. Behrend[29], J. Desmars[2], E. Meza[2], A. Alvarez-Candal[3], W. Beisker[30], A. R. Gomes-Junior[28], B. E. Morgado[3], F. Roques[2], F. Vachier[26], J. Berthier[26], T. G. Mueller[6], J. M. Madiedo[31], O. Unsalan[32], E. Sonbas[33], N. Karaman[33], O. Erece[34], D. T. Koseoglu[34], T. Ozisik[34], S. Kalkan[35], Y. Guney[36], M. S. Niaei[37], O. Satir[37], C. Yesilyaprak[37,38], C. Puskullu[39], A. Kabas[39], O. Demircan[39], J. Alikakos[40], V. Charmandaris[40,41], G. Leto[42], J. Ohlert[43,44], J. M. Christille[18], R. Szakáts[10], A. Takácsné Farkas[10], E. Varga-Verebélyi[10], G. Marton[10], A. Marciniak[45], P. Bartczak[45], T. Santana-Ros[45], M. Butkiewicz-Bąk[45], G. Dudziński[45], V. Alí-Lagoa[6], K. Gazeas[46], L. Tzouganatos[46], N. Paschalis[47], V. Tsamis[48], A. Sánchez-Lavega[49], S. Pérez-Hoyos[49], R. Hueso[49], J. C. Guirado[50,51], V. Peris[50] & R. Iglesias-Marzoa[52,53]

Haumea—one of the four known trans-Neptunian dwarf planets—is a very elongated and rapidly rotating body[1–3]. In contrast to other dwarf planets[4–6], its size, shape, albedo and density are not well constrained. The Centaur Chariklo was the first body other than a giant planet known to have a ring system[7], and the Centaur Chiron was later found to possess something similar to Chariklo's rings[8,9]. Here we report observations from multiple Earth-based observatories of Haumea passing in front of a distant star (a multi-chord stellar occultation). Secondary events observed around the main body of Haumea are consistent with the presence of a ring with an opacity of 0.5, width of 70 kilometres and radius of about 2,287 kilometres. The ring is coplanar with both Haumea's equator and the orbit of its satellite Hi'iaka. The radius of the ring places it close to the 3:1 mean-motion resonance with Haumea's spin period—that is, Haumea rotates three times on its axis in the time that a ring particle completes one revolution. The occultation by the main body provides an instantaneous elliptical projected shape with axes of about 1,704 kilometres and 1,138 kilometres. Combined with rotational light curves, the occultation constrains the three-dimensional orientation of Haumea and its triaxial shape, which is inconsistent with a homogeneous body in hydrostatic equilibrium. Haumea's largest axis is at least 2,322 kilometres, larger than previously thought, implying an upper limit for its density of 1,885 kilograms per cubic metre and a geometric albedo of 0.51, both smaller than previous estimates[1,10,11]. In addition, this estimate of the density of Haumea is closer to that of Pluto than are previous estimates, in line with expectations. No global nitrogen- or methane-dominated atmosphere was detected.

Within our programme of physical characterization of trans-Neptunian objects (TNOs), we predicted an occultation of the star URAT1 533—182543 by the dwarf planet (136108) Haumea and arranged observations as explained in Methods. Positive occultation detections were obtained on 21 January 2017, from twelve telescopes at ten different observatories. The instruments and the main features of each station are listed in Table 1.

As detailed in Methods (see also Fig. 1), the light curves (the normalized flux from the star plus Haumea versus time) show deep

---

[1] Instituto de Astrofísica de Andalucía (CSIC), Glorieta de la Astronomía S/N, 18008-Granada, Spain. [2] LESIA, Observatoire de Paris, PSL Research University, CNRS, Sorbonne Universités, UPMC Universités Paris 06, Universités Paris Diderot, Sorbonne Paris Cité, France. [3] Observatório Nacional/MCTIC, Rua General José Cristino 77, Rio de Janeiro CEP 20921-400, Brazil. [4] Federal University of Technology-Paraná (UTFPR/DAFIS), Rua Sete de Setembro 3165, CEP 80230-901 Curitiba, Brazil. [5] Universitäts-Sternwarte München, München, Scheiner Straße 1, D-81679 München, Germany. [6] Max-Planck-Institut für Extraterrestrische Physik, D-85741 Garching, Germany. [7] Dipartimento di Fisica e Astronomia, 'G. Galilei', Università degli Studi di Padova, Vicolo dell'Osservatorio 3, I-35122 Padova, Italy. [8] INAF—Osservatorio Astronomico di Padova, vicolo dell'Osservatorio 5, I-35122 Padova, Italy. [9] Dipartimento di Fisica, University of Padova, via Marzolo 8, 35131 Padova, Italy. [10] Konkoly Observatory, Research Centre for Astronomy and Earth Sciences, Hungarian Academy of Sciences, Konkoly Thege 15-17, H-1121 Budapest, Hungary. [11] Astronomical Institute, Slovak Academy of Sciences, 059 60 Tatranská Lomnica, Slovakia. [12] Astronomical Institute, Academy of Sciences of the Czech Republic, Fričova 298, 251 65 Ondřejov Czech Republic. [13] Astronomical Observatory San Marcello Pistoiese CARA Project, San Marcello Pistoiese, Pistoia, Italy. [14] Osservatorio astronomico di Tavolaia, Santa Maria a Monte, Italy. [15] Lajatico Astronomical Centre, Via Mulini a Vento 9 Orciatico, cap 56030 Lajatico, Italy. [16] Osservatorio Astronomico di Monte Agliale, Via Cune Motrone, I-55023 Borgo a Mozzano, Italy. [17] Črni Vrh Observatory, Predgriže 29A, 5274 Črni Vrh nad Idrijo, Slovenia. [18] Astronomical Observatory of the Autonomous Region of the Aosta Valley (OAVdA), Lignan 39, 11020 Nus, Italy. [19] Bayerische Volkssternwarte München, Rosenheimer Straße 145h, D-81671 München, Germany. [20] German Aerospace Center (DLR), Institute of Planetary Research, Rutherfordstraße 2, 12489 Berlin, Germany. [21] Departamento de Física, Ingeniería de Sistemas y Teoría de la Señal, Universidad de Alicante, PO Box 99, E-03080 Alicante, Spain. [22] Instituto Universitario de Física Aplicada a las Ciencias y la Tecnología, Universidad de Alicante, PO Box 99, E-03080 Alicante, Spain. [23] University of Zagreb, Faculty of Electrical Engineering and Computing, Department of Applied Physics, Unska 3, 10000 Zagreb, Croatia. [24] Ruđer Bošković Institute, Bijenička cesta 54, 10000 Zagreb, Croatia. [25] European Southern Observatory, Karl-Schwarzschild-Straße 2, 85748 Garching bei München, Germany. [26] IMCCE/Observatoire de Paris, 77 Avenue Denfert Rochereau, 75014 Paris, France. [27] Laboratório Interinstitucional de e-Astronomia-LIneA, Rua General José Cristino 77, Rio de Janeiro CEP 20921-400, Brazil. [28] Observatório do Valongo/UFRJ, Ladeira Pedro Antônio 43, Rio de Janeiro CEP 20080-090, Brazil. [29] Observatoire de Genève, CH1290 Sauverny, Switzerland. [30] International Occultation Timing Association—European Section (IOTA-ES) Bartold-Knausstraße 8, D-30459 Hannover, Germany. [31] Facultad de Ciencias Experimentales, Universidad de Huelva, Avenida de las Fuerzas Armadas, 21071 Huelva, Spain. [32] Ege University, Faculty of Science, Department of Physics, 35100 Izmir, Turkey. [33] University of Adiyaman, Department of Physics, 02040 Adiyaman, Turkey. [34] TUBITAK National Observatory (TUG), Akdeniz University Campus, 07058 Antalya, Turkey. [35] Ondokuz Mayis University Observatory, Space Research Center, 55200 Kurupelit, Turkey. [36] Atatürk University, Science Faculty, Department of Physics, 25240 Erzurum, Turkey. [37] Atatürk University, Astrophysics Research and Application Center (ATASAM), 25240 Erzurum, Turkey. [38] Atatürk University, Science Faculty, Department of Astronomy and Astrophysics, 25240 Erzurum, Turkey. [39] Canakkale Onsekiz Mart University, Astrophysics Research Center (ARC) and Ulupınar Observatory (UPO), Canakkale, Turkey. [40] Institute for Astronomy, Astrophysics, Space Applications and Remote Sensing, National Observatory of Athens, GR-15236 Penteli, Greece. [41] Department of Physics, University of Crete, GR-71003 Heraklion, Greece. [42] INAF—Catania Astrophysical Observatory, Via Santa Sofia 78, I-95123 Catania, Italy. [43] Michael Adrian Observatorium, Astronomie Stiftung Trebur, Fichtenstraße 7, 65468 Trebur, Germany. [44] University of Applied Sciences, Technische Hochschule Mittelhessen, Wilhelm-Leuschner-Straße 13, D-61169 Friedberg, Germany. [45] Astronomical Observatory Institute, Faculty of Physics, A. Mickiewicz University, Słoneczna 36, 60-286 Poznań, Poland. [46] Section of Astrophysics, Astronomy and Mechanics, Department of Physics, National and Kapodistrian University of Athens, GR-15784 Athens, Greece. [47] Nunki Observatory, Skiathos Island 37002, Greece. [48] Ellinogermaniki Agogi Observatory, Dimitriou Panagea street, GR-15351 Athens, Greece. [49] Departamento de Física Aplicada I, Escuela de Ingeniería de Bilbao, Universidad del País Vasco UPV/EHU, Plaza Torres Quevedo 1, 48013 Bilbao, Spain. [50] Observatori Astronòmic de la Universitat de València, Catedrático José Beltrán, 2, 46980 Paterna, Spain. [51] Departament d'Astronomia i Astrofísica, Universitat de València, Calle Dr Moliner 50, E-46100 Burjassot, Spain. [52] Centro de Estudios de Física del Cosmos de Aragón, Plaza de San Juan 1, 2ª planta, 44001 Teruel, Spain. [53] Departamento de Astrofísica, Universidad de La Laguna, Avenida Astrofísico Fco Sánchez, 38200 La Laguna, Spain.

Table 1 | Details of the observations on 21 January 2017

Site	Coordinates	Telescope aperture, filter and observer	Detector/instrument, exposure time and cycle time	Ingress and egress times (UT)
Skalnate Pleso Observatory, Slovakia (S)	49° 11′ 21.8″ N 20° 14′ 02.1″ E 1,826 m	1.3 m No filter R.K.	Moravian G4-9000 10 s 15.5 s	3:08:26.79 ± 0.96 3:10:24.56 ± 0.8
Konkoly Observatory, Hungary (K)	47° 55′ 01.6″ N 19° 53′ 41.5″ E 935 m	1.0 m No filter A.P.	Andor iXon-888 1 s 1.007 s	3:08:20.3 ± 0.2 3:10:17.39 ± 0.07
Konkoly Observatory, Hungary (K)	47° 55′ 01.6″ N 19° 53′ 41.5″ E 935 m	0.6 m No filter A.P.	Apogee Alta U16HC 2 s 2.944 s	3:08:19.5 ± 0.8 3:10:16.4 ± 1.3
Ondrejov Observatory, Czech Republic (O)	49° 54′ 32.6″ N 14° 46′ 53.3″ E 526 m	0.65 m No filter K.H.	Moravian G2-3200 8 s 9.721 s	3:08:29.2 ± 0.8 3:10:12.2 ± 0.8
Crni Vrh Observatory, Slovenia (CV)	45° 56′ 45.0″ N 14° 04′ 15.9″ E 713 m	0.6 m Clear H.M.	Apogee Alta U9000HC 300 s, drifted 315 s	3:07:54 ± 8 3:09:57 ± 10
Wendelstein Observatory, Germany (W)	47° 42′ 13.6″ N 12° 00′ 44.0″ E 1,838 m	2.0 m r′ C.R.	WWFI 10 s 14.536 s	3:08:27.9 ± 2.8 3:09:34.1 ± 0.5
Wendelstein Observatory, Germany (W)	47° 42′ 13.6″ N 12° 00′ 44.0″ E 1,838 m	0.4 m r′ C.R.	SBIG ST10-XME 30 s 53.096 s	3:08:18.8 ± 6 3:09:38.6 ± 6
Bavarian Public Observatory, Munich, Germany (M)	48° 07′ 19.2″ N 11° 36′ 25.2″ E 538 m	0.8 m No filter B.G.	ATIK 314L+ 20 s 20.304 s	3:08:30.0 ± 3.3 3:09:30.0 ± 4.9
Asiago Observatory, Cima Ekar, Italy (As)	45° 50′ 54.9″ N 11° 34′ 08.4″ E 1,376 m	1.82 m No filter V.G.	AFOSC 2 s 5.026 s	3:08:20.17 ± 0.08 3:09:13.27 ± 1.5
San Marcello Pistoiese Observatory, Italy (SMP)	44° 03′ 51.0″ N 10° 48′ 14.0″ E 965 m	0.6 m No filter P. Bacci, M.M., L.N. and L.M.	Apogee Alta U6 10 s 11.877 s	3:08:22.9 ± 0.9 3:08:42.8 ± 0.9
Lajatico Astronomical Centre, Italy (L)	43° 25′ 44.7″ N 10° 43′ 01.2″ E 433 m	0.5 m No filter M.B., F. Martinelli, G.S.	Moravian G3-1000 15 s 16.254 s	3:08:19.9 ± 1.4 3:08:34.3 ± 1.4
Mount Agliale Observatory, Italy (Ag)	43° 59′ 43.1″ N 10° 30′ 53.8″ E 758 m	0.5 m No filter F.C.	FLI proline 4710 15 s 16.724 s	*

The table shows the observing sites from which the most relevant observations were obtained, the main parameters of the observations for each site and the derived disappearance (ingress) and reappearance (egress) times of the star caused by the central body, using the square-well-model fits in Fig. 1. The cycle times are the times between consecutive exposures. At Wendelstein Observatory and Konkoly Observatory, two different telescopes were used; hence there are 12 detections of the occultation from 10 different sites. Weather was clear at all of the stations except at the Bavarian Public Observatory (Munich), where intermitent clouds were present.

*The occultation by the main body of Haumea was not detectable from Mount Agliale; only ring events were detected. See Methods and Extended Data Table 2.

drops caused by Haumea near the predicted time (around 3:09 UT). Because the drops are abrupt, Haumea must lack a global Pluto-like atmosphere. An upper limit on the surface pressure of a nitrogen- or methane-dominated atmosphere is determined to be 15 nbar and 50 nbar, respectively, at the 3σ level.

Square-well fits to the drops provide the times of star disappearance and reappearance at each site. Those times define an occultation chord for each site, and an elliptical fit to the extremities of the chord provides the instantaneous limb of Haumea, with values of $1{,}704 \pm 4$ km and $1{,}138 \pm 26$ km for the major and minor axes of the ellipse (Fig. 2). The position angle of the minor axis is $-76.3° \pm 1.2°$.

In addition to the main occultation, there are brief dimmings before and after the main event. These dips are consistently explained by a narrow and dense ring around Haumea that absorbed about 50% of the incoming stellar flux. This ring has reflectivity similar to those found around the Centaurs Chariklo[7] and Chiron[8,9] and around Uranus[12] and Neptune[13]. From an elliptical fit to the positions of those brief events (projected in the plane of the sky), we obtain an apparent semi-major axis of $a'_{\mathrm{ring}} = 2{,}287^{+75}_{-45}$ km and apparent semi-minor axis of $b'_{\mathrm{ring}} = 541 \pm 15$ km for the ring (the error here and elsewhere stems from the uncertainty in the timing of the events, see Fig. 3) The position angle of the apparent minor axis of the ring is $P_{\mathrm{ring}} = -74.3° \pm 1.3°$, which coincides with that of the fit of Haumea's limb to within error bars, suggesting that the ring lies in Haumea's equatorial plane; see below.

Under the assumption that the ring ellipse seen in Fig. 3 corresponds to the projection of a circular ring, we derive a ring opening angle of $B_{\mathrm{ring}} = \arcsin(b'_{\mathrm{ring}}/a'_{\mathrm{ring}}) = 13.8° \pm 0.5°$ ($B_{\mathrm{ring}} = 0°$ corresponds to an edge-on geometry). A ring particle orbiting a triaxial body with semi-axes $a > b > c$ that rotates around the axis c has its average angular momentum H_c along c conserved. In this case, the state of least energy for a collisional, dissipative disk with constant H_c is an equatorial ring. Therefore, Haumea's equator should also be observed under the angle 13.8°. This is consistent with the high amplitude of its rotational light curve, which requires low values of B (ref. 1). The values of P_{ring} and B_{ring} provide two possible solutions for the ring pole, with J2000 equatorial coordinates $(\alpha_{\mathrm{p}}, \delta_{\mathrm{p}}) = (285.1° \pm 0.5°, -10.6° \pm 1.2°)$ (solution 1) and $(\alpha_{\mathrm{p}}, \delta_{\mathrm{p}}) = (312.3° \pm 0.3°, -18.6° \pm 1.2°)$ (solution 2). Solution 1 is preferred, because it is consistent with the long-term photometric behaviour of Haumea and because it is coincident, to within error bars, with the orbital pole position of Haumea's main satellite, Hi'iaka, $(\alpha_{\mathrm{p}}, \delta_{\mathrm{p}}) = (283.0° \pm 0.2°, -10.6° \pm 0.7°)$ (ref. 14). In that context, both the ring and Hi'iaka would lie in Haumea's equatorial plane.

At about 2,287 km from Haumea's centre, the ring is within the Roche limit of a fluid-like satellite, which corresponds to about 4,400 km for a spherical Haumea (using a density of 1,885 kg m^{-3} for the primary and a density of 500 kg m^{-3} for the satellite). When the elongated shape of Haumea is considered, the Roche limit is even further out. Hence, the ring is close enough to Haumea that accretion cannot proceed to form a satellite. The ring is close to the 3:1 spin–orbit resonance with Haumea, a ring particle undergoing one revolution while Haumea completes three rotations. This resonance occurs at $2{,}285 \pm 8$ km (see Methods). More knowledge of the ring orbit and of the internal structure of Haumea (which may be not homogeneous, see below) will be required to show whether this proximity is coincidental or the ring is actually trapped into

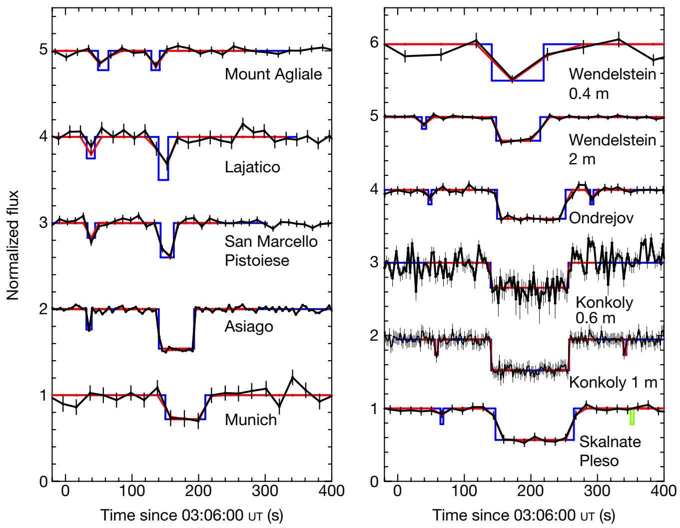

Figure 1 | Light curves of the occultation. Light curves in the form of normalized flux versus time (at mid-exposure) were obtained from the different observatories that recorded the occultation (Table 1). The black points and lines represent the light curves extracted from the observations. The blue lines show the best square-well-model fits to the main body and the ring at Konkoly, with square-well models derived from the assumed ring width and opacity ($W = 70$ km and $p' = 0.5$) at other sites. The red points and lines correspond to the optimal synthetic profile deduced from the square-well model fitted at each data point (see Methods). The rectangular profile in green corresponds to the ring egress event at Skalnate Pleso, which fell in a readout time of the camera (see Fig. 3). The light curves have been shifted in steps of 1 vertically for better viewing. 'Munich' corresponds to the Bavarian Public Observatory. Error bars are 1σ.

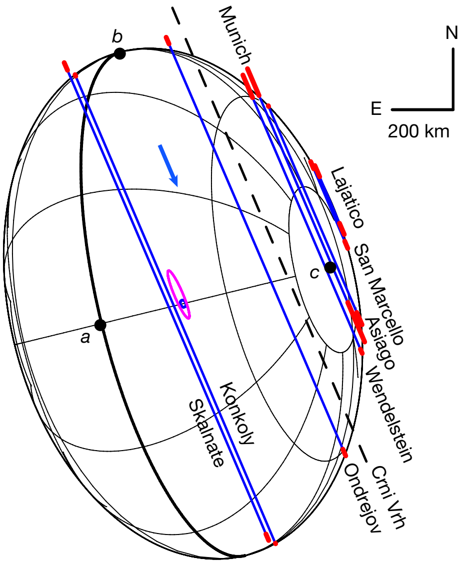

Figure 2 | Haumea's projected shape. The blue lines are the occultation chords of the main body projected onto the sky plane, as seen from nine observing sites (Table 1). The red segments are the uncertainties (1σ level) on the extremites of each chord, as derived from the timing uncertainties in Table 1. We show the chord from Crni Vrh in dashed line because it is considerably uncertain. For the observatories for which two telescopes were used we show only the best chord. Celestial north ('N') and east ('E') are indicated in the upper right corner, together with the scale. The blue arrow shows the motion of the star relative to the body. Haumea's limb (assumed to be elliptical) has been fitted to the chords, accounting for the uncertainties on the extremity of each chord (red segments). The limb has semi-major axis $a' = 852 \pm 2$ km and semi-minor axis $b' = 569 \pm 13$ km, the latter having a position angle $P_{\mathrm{limb}} = -76.3° \pm 1.2°$ counted positively from the celestial north to the celestial east. Haumea's equator has been drawn assuming that it is coplanar with the ring, with planetocentric elevation $B_{\mathrm{ring}} = 13.7° \pm 0.5°$; see Fig. 3. The pink ellipse indicates the 1σ-level uncertainty domain for the ring centre, and the blue ellipse inside it is the corresponding domain for Haumea's centre. To within error bars, the ring and Haumea's centres (separated by 33 km in the sky plane) cannot be distinguished, indicating that our data are consistent with a circular ring concentric with the dwarf planet. The points labelled '*a*', '*b*' and '*c*' indicate the intersections of the *a*, *b* and *c* semi-axes of the modelled ellipsoid with Haumea's surface.

this resonance, and if the latter, for what reason. However, answering these questions remains out of reach of the present work.

Another important property of Haumea is its geometric albedo (p_V), which can be determined using its projected area, as derived from the occultation, and its absolute magnitude[15]. We find a geometric albedo $p_V = 0.51 \pm 0.02$, which is considerably smaller than the values of 0.7–0.75 and $0.804^{+0.062}_{-0.095}$ derived from the latest combination of Herschel and Spitzer thermal measurements[8,16]. The geometric albedo should be even smaller if the contributions of the satellites and the ring to the absolute magnitude are larger than the 13.5% used here (see Methods).

Because Haumea is thought to have a triaxial ellipsoid shape[1,17,18] with semi-axes $a > b > c$, the occultation alone cannot provide its three-dimensional shape unless we use additional information from the rotational light curve. From measurements performed in the days before and after the occultation, and given that we know Haumea's rotation period with high precision[16], we determined the rotational phase at the occultation time. It turns out that Haumea was at its absolute brightness minimum, which means that the projected area of the body was at its minimum during the occultation.

The magnitude change from minimum to maximum absolute brightness determined from the Hubble Space Telescope is 0.32 mag (using images that separated Haumea and Hi'iaka[7]). Using equation (5) in ref. 19 together with the aspect angle in 2009 (when the observations were taken[7]) and the occultation ellipse parameters, we derive the following values for the semi-axes of the ellipsoid: $a = 1{,}161 \pm 30$ km, $b = 852 \pm 4$ km and $c = 513 \pm 16$ km (see Methods). The resulting density of Haumea, using its known mass[20], is $1{,}885 \pm 80$ kg m^{-3}, and its volume-equivalent diameter is $1{,}595 \pm 11$ km. This diameter is determined under the assumption that the ring does not contribute to the total brightness. For an upper limit of 5% contribution (see Methods), the real amplitude of the rotational light curve increases, and hence the a semi-axis increases too. The volume-equivalent diameter in this case is 1,632 km and the density is 1,757 kg m^{-3}. These two densities are considerably smaller than the lower limit of 2,600 kg m^{-3} based on the figures of hydrostatic equilibrium, or on mass and previous volume determinations[1]. A value in the range 1,885–1,757 kg m^{-3} is far more in line with the density of other large TNOs and in agreement with the trend of increasing density versus size (see, for example, supplementary information in ref. 5, and refs 21 and 22). We also note that the axial ratios derived from the occultation are not consistent with those expected from the hydrostatic equilibrium figures of a homogeneous body[23] for the known rotation rate and the derived density. It has previously been hypothesized[24] that the density of Haumea could be much smaller than the minimum value of 2,600 kg m^{-3} reported previously, if granular physics is used to model the shape of the body instead of the simplifying assumption of fluid behaviour. From figure 4 of ref. 25, we determine an approximate angle of friction of between 10° and 15° for Haumea given the c/a ratio of about 0.4 that we determined here. For reference, the maximum angle of friction of solid rocks on Earth is 45° and that of a fluid is 0°. Also, differentiation and other effects may have an important role in determining the final shape[26].

Chariklo, a body of around 250 km in diameter with a Centaur orbit (between the orbits of Jupiter and Neptune), was the first Solar System object other than the giant planets found to have a ring system[7]. Shortly after that discovery, similar occultation features that resembled those from Chariklo's rings were found on Chiron[8,9], another Centaur. These discoveries directed our attention to Centaurs and phenomenology related to them to explain our unexpected findings. The discovery of

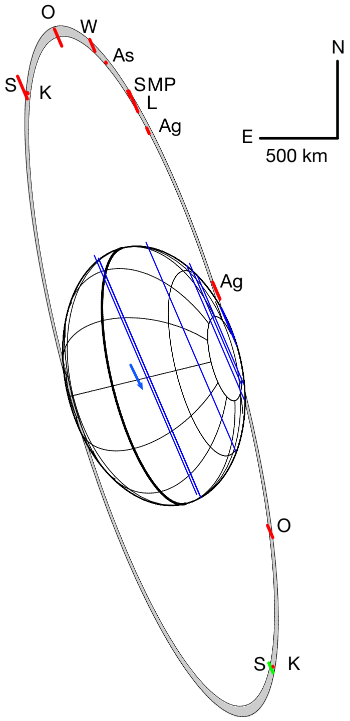

Figure 3 | Haumea's ring geometry. The figure shows a fit to the ring events (red segments), with the other features the same as in Fig. 2. Those segments show the 1σ uncertainty intervals for the midtimes of the secondary events at Mount Agliale (Ag), Lajatico (L), San Marcello Pistoiese (SMP), Asiago (As), Wendelstein (W), Ondrejov (O), Konkoly (K) and Skalnate Pleso (S). No ring event could be detected from the Bavarian Public Observatory (in Munich) because of the low signal-to-noise ratio. The ring egresses at Wendelstein, Asiago, San Marcello Pistoiese and Lajatico are not observed because they are blocked by the main body. At Skalnate Pleso, the ring egress is not detected (despite the high signal-to-noise ratio of the data) either because the ring is not homogeneous or because its egress is lost in the readout time (marked here in green). The latter is the most likely explanation because the readout times of 5.5 s were long compared to the integration time of 10 s. Also, the green segment is very close to the positive Konkoly detection, making the hypothesis of an inhomogeneous ring unlikely. The two ellipses around Haumea delineate a 70-km-wide ring with an apparent opacity of 0.5 (grey area) and semi-major axis of $a_{\rm ring} = 2,287^{+75}_{-45}$ km that best simultaneously fits the secondary events of Fig. 1. The ring fit provides an opening angle $B_{\rm ring} = 13.8° \pm 0.5°$ and a position angle for the apparent minor axis of the ring of $P_{\rm ring} = -74.3° \pm 1.3°$. This is aligned, to within error bars, with Haumea's apparent minor axis $P_{\rm limb} = -76.3° \pm 1.2°$ (Fig. 2). Moreover, the orbital pole position of Hi'iaka[14] implies a sub-observer elevation of $B_{\rm Hi'iaka} = -15.7°$ above the orbit of Hi'iaka on 2017 January 21 and a superior conjunction occurring at a position angle of $P_{\rm Hi'iaka} = -73.6°$. The fact that $|B_{\rm ring}| \approx |B_{\rm Hi'iaka}|$ and $P_{\rm ring} \approx P_{\rm limb} \approx P_{\rm Hi'iaka}$ strongly suggests that the ring and Hi'iaka both orbit in Haumea's equatorial plane.

a ring around Haumea—a much more distant body, in a completely different dynamical class, much larger than Chariklo and Chiron, with satellites and with a very elongated triaxial shape—has numerous implications, such as rings being possibly common also in the trans-Neptunian region from which Centaurs are delivered, and opens the door to new avenues of research.

Online Content Methods, along with any additional Extended Data display items and Source Data, are available in the online version of the paper; references unique to these sections appear only in the online paper.

Received 4 June; accepted 30 August 2017.

1. Rabinowitz, D. L. *et al.* Photometric observations constraining the size, shape, and albedo of 2003 EL61, a rapidly rotating, Pluto-sized object in the Kuiper belt. *Astrophys. J.* **639,** 1238–1251 (2006).
2. Brown, M. E. *et al.* Keck observatory laser guide star adaptive optics discovery and characterization of a satellite to the large Kuiper belt object 2003 EL_{61}. *Astrophys. J.* **632,** L45–L48 (2005).
3. Brown, M. E., Barkume, K. M., Ragozzine, D. & Schaller, E. L. A collisional family of icy objects in the Kuiper belt. *Nature* **446,** 294–296 (2007).
4. Sicardy, B. *et al.* A Pluto-like radius and a high albedo for the dwarf planet Eris from an occultation. *Nature* **478,** 493–496 (2011).
5. Ortiz, J. L. *et al.* Albedo and atmospheric constraints of dwarf planet Makemake from a stellar occultation. *Nature* **491,** 566–569 (2012).
6. Stern, S. A. *et al.* The Pluto system: initial results from its exploration by New Horizons. *Science* **350,** aad1815 (2015).
7. Braga-Ribas, F. *et al.* A ring system detected around the Centaur (10199) Chariklo. *Nature* **508,** 72–75 (2014).
8. Ortiz, J. L. *et al.* Possible ring material around Centaur (2060) Chiron. *Astron. Astrophys.* **576,** A18 (2015).
9. Ruprecht, J. *et al.* 29 November 2011 stellar occultation by 2060 Chiron: symmetric jet-like features. *Icarus* **252,** 271–276 (2015).
10. Lockwood, A. C., Brown, M. E. & Stansberry, J. The size and shape of the oblong dwarf planet Haumea. *Earth Moon Planets* **111,** 127–137 (2014).
11. Fornasier, S. *et al.* TNOs are cool: a survey of the trans-Neptunian region. VIII. Combined Herschel PACS and SPIRE observations of nine bright targets at 70–500 μm. *Astron. Astrophys.* **555,** A15 (2013).
12. Elliot, J. L., Dunham, E. & Mink, D. The rings of Uranus. *Nature* **267,** 328–330 (1977).
13. Hubbard, W. B. *et al.* Occultation detection of a Neptunian ring-like arc. *Nature* **319,** 636–640 (1986).
14. Gourgeot, F. *et al.* Near-infrared spatially resolved spectroscopy of (136108) Haumea's multiple system. *Astron. Astrophys.* **593,** A19 (2016).
15. Rabinowitz, D. L., Schaefer, B. E. & Tourtellotte, S. W. The diverse solar phase curves of distant icy bodies. I. Photometric observations of 18 trans-Neptunian objects, 7 Centaurs, and Nereid. *Astron. J.* **133,** 26–43 (2007).
16. Lellouch, E. *et al.* "TNOs are cool": a survey of the trans-Neptunian region. II. The thermal lightcurve of (136108) Haumea. *Astron. Astrophys.* **518,** L147 (2010).
17. Lacerda, P., Jewitt, D. & Peixinho, N. High-precision photometry of extreme KBO 2003 EL_{61}. *Astron. J.* **135,** 1749–1756 (2008).
18. Thirouin, A. *et al.* Short-term variability of a sample of 29 trans-Neptunian objects and Centaurs. *Astron. Astrophys.* **522,** A93 (2010).
19. Binzel, R. P., Farinella, P., Zappala, V. & Cellino, A. in *Asteroids II* (eds Binzel, R. P. *et al.*) 416–441 (Univ. Arizona Press, 1989).
20. Ragozzine, D. & Brown, M. E. Orbits and masses of the satellites of the dwarf planet Haumea (2003 EL61). *Astron. J.* **137,** 4766–4776 (2009).
21. Carry, B. Density of asteroids. *Planet. Space Sci.* **73,** 98–118 (2012).
22. Stansberry, J. A. *et al.* Physical properties of trans-Neptunian binaries (120347) Salacia-Actaea and (42355) Typhon-Echidna. *Icarus* **219,** 676–688 (2012).
23. Chandrasekhar, S. *Ellipsoidal Figures of Equilibrium* (Dover, 1987).
24. Holsapple, K. A. Spin limits of Solar System bodies: from the small fast-rotators to 2003 EL61. *Icarus* **187,** 500–509 (2007).
25. Holsapple, K. A. Equilibrium configurations of solid cohesionless bodies. *Icarus* **154,** 432–448 (2001).
26. Rambaux, N., Chambat, F., Castillo-Rogez, J. & Baguet D. Equilibrium figures of dwarf planets. In *AAS/Division of Planetary Sciences Meeting* Vol. 48, abstr. 120.15 (American Astronomical Society, 2016).

Acknowledgements These results were based on observations made with the 2-m telescope at Wendelstein Observatory, which is operated by the Universitäts-Sternwarte München, the 1.8-m telescope at Asiago Observatory, operated by Padova Observatory, a member of the National Institute for Astrophysics, the 1.3-m telescope at Skalnate Pleso Observatory, operated by the Astronomical Institute of the Slovak Academy of Science, the 1-m telescope at Konkoly observatory, operated by Astrophysical Institute of the Hungarian Academy of Sciences, the 0.65-m telescope at Ondrejov Observatory, operated by the Astronomical Institute of the Czech Academy of Sciences, the 1.5-m telescope at Sierra Nevada Observatory, operated by the Instituto de Astrofisica de Andalucia-CSIC, the 1.23-m telescope at Calar Alto Observatory, jointly operated by the Max Planck Institute für Astronomie and the IAA-CSIC, the Roque de los Muchachos Observatory 2-m Liverpool telescope, operated by the Astrophysics Research Institute of Liverpool John Moores University, the Roque de los Muchachos Observatory 2.5-m NOT telescope, operated by the Nordic Optical Telescope Scientific Association, the 1-m telescope at Pic du Midi Observatory, operated by the Observatoire Midi Pyrénées, and the La Hita 0.77-m telescope, which is jointly operated by Astrohita and the IAA-CSIC. J.L.O. acknowledges funding from Spanish and Andalusian grants MINECO AYA-2014-56637-C2-1-P and J. A. 2012-FQM1776 as well as FEDER funds. Part of the research leading to these results received funding from the European Union's Horizon 2020 Research and Innovation Programme, under grant agreement no. 687378. B.S. acknowledges support from the French grants 'Beyond Neptune' ANR-08-BLAN-0177 and 'Beyond Neptune II' ANR-11-IS56-0002. Part of the research leading to these results has received funding from the European Research Council under the European Community's H2020 (2014-2020/ERC grant agreement no. 669416 'Lucky Star'). A.P. and R.S. have been supported by the grant LP2012-31 of the Hungarian Academy of Sciences. All of the Hungarian contributors acknowledge the partial support from K-125015 grant of the National Research, Development and Innovation Office (NKFIH). G.B.-R., F.B.-R., F.L.R., R.V.-M., J.I.B.C., M.A., A.R.G.-J. and B.E.M. acknowledge support from CAPES, CNPq and FAPERJ. J.C.G. acknowledges funding from AYA2015-63939-C2-2-P and from the Generalitat Valenciana PROMETEOII/2014/057. K.H. and P.P. were supported by the project RVO:67985815. The Astronomical Observatory of the Autonomous Region of the Aosta Valley acknowledges a Shoemaker NEO Grant 2013 from The Planetary Society. We acknowledge funds from a 2016 'Research and Education' grant from Fondazione CRT. We also acknowledge the Slovakian project ITMS no. 26220120029.

Author Contributions J.L.O. planned the campaign, analysed data for the prediction, made the prediction, participated in the observations, obtained and analysed data, interpreted the data and wrote the paper. P.S.-S. helped to plan the campaign, analysed data, helped to interpret the data and helped to write the paper. B.S. helped to plan the campaign, analysed data, interpreted data, and wrote part of the paper. G.B.-R. and D.B. helped to plan the campaign, participated in the observations, and analysed and interpreted data. All other authors participated in the planning of the campaign and/or the observations and/or the interpretations. All authors were given the opportunity to review the results and comment on the manuscript.

Author Information Reprints and permissions information is available at www.nature.com/reprints. The authors declare no competing financial interests. Readers are welcome to comment on the online version of the paper. Publisher's note: Springer Nature remains neutral with regard to jurisdictional claims in published maps and institutional affiliations. Correspondence and requests for materials should be addressed to J.L.O. (ortiz@iaa.es).

Reviewer Information *Nature* thanks A. Sickafoose and A. Verbiscer for their contribution to the peer review of this work.

METHODS

Occultation predictions. The occultation was predicted in late 2015 by using the URAT1 star catalogue and several ephemeris sources for Haumea. Because the star involved in the occultation (URAT1 533−182543) was sufficiently bright ($m_\mathrm{R} \approx 17.7$), the event had the potential to be detectable from numerous sites. The initial predictions based on a JPL orbit (obtained at the JPL horizons website; http://ssd.jpl.nasa.gov/horizons.cgi) put the shadow path slightly outside Earth. Other ephemeris sources such as Astorb (ftp://ftp.lowell.edu/pub/elgb/astorb.html) and NIMA[27] were more favourable, giving rise to shadow paths well within Earth. The scatter in the predictions, owing to the uncertainty in Haumea's orbit, was of the order of 300 milliarcseconds (mas). Given that Haumea's angular diameter was expected to be much smaller than that, refined predictions were needed to make sure that a detection could be made. Besides, the presence of a large satellite (Hi'iaka) orbiting Haumea could cause an astrometric wobble similar to that detected in the system of Orcus and its satellite Vanth[28] due to the photocentre oscillation around the barycentre of the system.

Hence, we decided to carry out a detailed astrometric monitoring of Haumea. More than 1,000 measurements of Haumea's position were obtained with the 0.77-m f/3 La Hita telescope from 1 April to 4 July 2016 using a 4,096 × 4,069 CCD (charge-coupled device) camera. The unfiltered images were taken on a daily basis (weather and moon permitting) when Haumea was near culmination to avoid possible differential chromatic refraction (DCR) problems as much as possible. The instrument, the image processing and the methodology were the same as those used for the prediction of the stellar occultation by Makemake[5]. The analysis of the data resulted in a shadow path favourable for locations in a wide region of Earth. Hence, this encouraged further work. Once the GaiaDR1 catalogue was released we improved our prediction with new coordinates of the occultation star by combining the position (epoch 2015.0) with the information on position and proper motions from URAT1 at its 2013.669 epoch and from other catalogues.

The final star coordinates (J2000) that we derived for the occultation epoch (2017.058) were right ascension $\alpha = 14$ h 12 min 03.2034 s and declination $\delta = +16°\ 33'\ 58.642''$. After the occultation, the HSOY catalogue[29] has become available, which provides coordinates and proper motions of GaiaDR1 stars matched with PPMXL stars. From this catalogue, the J2000 coordinates for epoch 2017.058 turn out to be $\alpha = 14$ h 12 min 03.2034 s, $\delta = +16°\ 33'\ 58.647''$, which agree completely in right ascension and differ by only 4 mas in declination.

Once the GaiaDR1 catalogue became available in September 2016 we also redid the Haumea astrometry from the entire La Hita 0.77-m telescope dataset with respect to GaiaDR1. Owing to the higher accuracy of GaiaDR1 with respect to previous catalogues of similar depth, the resulting astrometry showed a clear oscillation of the residuals to the JPL orbit with respect to the measurements (observed − calculated) due to the presence of the satellite Hi'iaka. A Lomb periodogram[30] of the residuals in declination showed its strongest peak at a significant periodicity of 49.5 ± 0.9 days, which coincides with the known[20] orbital period of Hi'iaka (49.462 ± 0.083 days). A sinusoidal fit to the residuals (Extended Data Fig. 1) using the orbital period of Hi'iaka had a maximum when the theoretical position of Hi'iaka was at its northernmost position with respect to Haumea, and the minimum of the fit corresponded to the southernmost position of the satellite Hi'iaka. Hence we verified that the oscillation was indeed correlated with the theoretical positions of Hi'iaka. For the theoretical computations of the Hi'iaka orbit we used the miriade ephemeris service (http://vo.imcce.fr/webservices/miriade/).

With that information we could already make a reliable prediction of the occultation for 21 January 2017 that indicated a favourable shadow path for central Europe. The resulting offsets with respect to JPL#81 orbit (with planetary ephemeris version DE431) were 174 mas and 73 mas in $\alpha\cos(\delta)$ and in declination, respectively. This represented the offset of the barycentre of Haumea's system with respect to the JPL#81 ephemerides. In early December 2016 we again took images of Haumea, and astrometrically solved them with respect to the GaiaDR1 catalogue. This time we used several larger telescopes (the Sierra Nevada Observatory 1.5-m telescope, the Calar Alto Observatory 1.2-m telescope, the Pic du Midi Observatory 1-m telescope, the 2-m Liverpool telescope and the 2.5-m Nordic Optical telescope to obtain observations of Haumea in R band). We determined the offsets of the astrometric measurements with respect to JPL ephemeris (observed − computed). Then we performed a correlation analysis of the offsets with respect to the computed theoretical positions of the satellite Hi'iaka and found offsets in α and δ for the position of the barycentre of the Haumea system with respect to the ephemerides. These offsets were determined from linear fits and are 176 ± 6 mas in $\alpha\cos(\delta)$ and 73 ± 11 mas in δ with respect to the JPL#81 orbit. The errors were determined from the uncertainties in the parameters of the linear fits. These offsets were in perfect agreement with those calculated with the large La Hita dataset. The Spearman correlation coefficients were 0.91 and 0.88 for the right ascension and declination residuals, respectively.

On the other hand, we determined the distance of Haumea with respect to the barycentre using $1{,}232/(1 + r)$, where 1,232 is the separation of Hi'iaka with respect to Haumea in milliarcseconds and r is the mass ratio of Haumea to Hi'iaka. That mass ratio was thought to be about 200, assuming similar albedos for Haumea and Hi'iaka (or even higher for Hi'iaka, given the depth of the water ice feature as shown in ref. 31). Projected in the plane of the sky, the offset position of Haumea on 21 January 2017 with respect to the barycentre was then calculated to be −6 mas in declination and 2 mas in $\alpha\cos(\delta)$. The predicted shadow path was favourable for Italy and central Europe. We decided to organize a campaign with observing sites from Spain to Turkey to maximize the chances of success and to compensate for possible systematic errors that could have not been accounted for.

A map of the final shadow path on Earth with the sites that played the key parts in the observations is shown in Extended Data Fig. 2. The centre of Haumea from the occultation was 17 mas and 16 mas away from the prediction, in $\alpha\cos(\delta)$ and δ, respectively. This translates into a difference of 409 km in the centerline of the shadow path and 55 s in time with respect to the prediction.

Occultation observations. Sequences of CCD images were acquired at each observing site listed in Table 1. At Wendelstein, a red r′ sloan filter was used, while all the other observatories used no filters to maximize the signal-to-noise ratio. Except for the Konkoly 1-m telescope observations, all of the image sequences had interruptions due to the non-negligible readout time of the cameras.

From the sequences of CCD images obtained at each telescope (and after standard dark-subtraction and flatfielding correction), light curves were constructed by carrying out synthetic aperture photometry of the occultation star (blended with Haumea) with respect to reference stars in the field of view. The synthetic aperture measurements were made using DAOPHOT routines and searching for the optimum aperture to minimize the scatter of the photometry. The photometry was performed relative to reference stars in the images so that small transparency fluctuations or seeing variations could be monitored and compensated for. The timing information was extracted from the time in the fits headers of the images. The time tagging accuracy at the different observatories (time tagging was done by synchronizing the controling computers with NTP time servers) is estimated to be 0.1 s on average. The main parameters of the star are shown in Extended Data Table 1. The brightness of the star was similar to that of Haumea, so at the time of the occultation we expected a brightness change of around 50% in the Haumea + star blended source. The resulting light curves (photon flux relative to the average value, versus time) are shown in Fig. 1.

The observations at Crni Vrh consisted of drifted images with 300 s of exposure time, tracked at a speed of 40″ per minute in the north–south direction. Hence, aperture photometry could not be made. The detailed analysis procedure for this dataset is explained in Methods section 'Analysis of the Crni Vrh images'.

Limb fit to the occultation chords. Square-well fits to the occultation profiles were performed to accurately determine the times of star disappearance and reappearance for each observatory (Table 1), except for Crni Vrh, for which a special technique was needed as explained in Methods section 'Analysis of the Crni Vrh images'. The methodology to fit square wells was the same as that in other work on stellar occultations[4,5,7,32] by TNOs. The main parameters of the model are the depth of the square well, and the disappearance and reappearance times of the occultation. The uncertainties in the retrieved parameters were obtained from a grid search in the parameter space. Acceptable values were those that gave a χ^2 within χ^2_min and $\chi^2_\mathrm{min} + 1$. The uncertainties are listed in Table 1. The errors from the time tagging accuracy were an order of magnitude smaller than the uncertainties arising from the fits. From the fitted times at the different sites, we can generate chords in the projected plane of the sky. We fitted an elliptical limb to the extremities of the chords by minimizing a χ^2 function:

$$\chi^2 = \sum_1^N \frac{(r_{i,\mathrm{obs}} - r_{i,\mathrm{cal}})^2}{\sigma_{i,r}^2} \qquad (1)$$

where r is the radius from the centre of the ellipse (f_c, g_c), 'cal' means calculated and 'obs' means observed; $\sigma_{i,r}$ are the errors of the extremities, which were derived from the errors in the retrieved ingress and egress times (using the known speed of Haumea), and N is the number of extremities. The retrieved a' and b' parameters (semi-axes of the fitted ellipse, not to be confused with the semi-axes of the triaxial ellipsoid, a, b and c) were translated from milliarcseconds into length in kilometres by using the known distance of Haumea from Earth (50.4847 AU). This is the same procedure followed in other stellar occultation studies of TNOs[4,5,7]. The parameters of the ellipse fit were 1,704 ± 4 km, 1,138 ± 26 km and $P_\mathrm{limb} = -76.3° \pm 1.2°$. The fit used 9 occulting chords, providing 18 data points along the limb, and returned the best-fitting value $\chi^2_\mathrm{min} = 18.6$. This value corresponds to a χ^2 per degree of freedom of 1.43, because we have 5 free parameters, which means that the fit is satisfactory.

Upper limit on the pressure of a putative atmosphere. Global atmospheres of the type seen in Pluto and other Solar System bodies cause a gradual star disappearance during occultations as well as a gradual reappearance. Upper limits on the pressure of a putative nitrogen-dominated or methane-dominated Pluto-like atmosphere can be derived from the occultation profiles; see below. Nitrogen and methane are the volatile ices that can sublimate at the distances from the sun at which Haumea is (50.593 AU). Even though there is no spectroscopic evidence of N_2 or CH_4 ices on Haumea's surface in substantial amounts[31], their presence below the surface cannot be completely discarded.

Here we use the best available dataset—the Asiago light curve—to derive Haumea's atmospheric upper limits (Fig. 1). From Haumea's mass of $(4.006 \pm 0.04) \times 10^{21}$ kg (ref. 20) and assuming that the body itself is in hydrostatic equilibrium we derive an average surface gravity of $0.39\,\mathrm{m\,s^{-2}}$.

We consider first a pure N_2 isothermal atmosphere in thermal balance with a surface temperature of 40 K (ref. 16). This provides a vertical density profile from which a ray-tracing code calculates synthetic light curves, once a surface pressure p_{surf} has been prescribed (see refs 4 and 5 for details). We define a χ^2 function in the same way as in equation (1), except that now p_{surf} is the adjusted parameter. We find that χ^2 is minimum for $p_{\mathrm{surf}} = 0$ (no atmosphere) and that it reaches $\chi^2_{\mathrm{min}} + 1$ for $p_{\mathrm{surf}}(N_2) = 3$ nbar, which sets the 1σ-level upper limit for a N_2 atmosphere. At 3σ the upper limit is 15 nbar. In Extended Data Fig. 3, we show the effect that a N_2 isothermal atmosphere would have on the observations.

A CH_4 atmosphere would be more difficult to detect using our dataset. This stems from the fact that near-infrared heating of methane would cause a thermal profile starting from a typical surface temperature of 40 K, then ramping up to typically 100 K in a few-kilometre-thick stratosphere (see discussion in ref. 5). Our dataset lacks sufficient spatial resolution to resolve such a thin layer, so a less constraining upper limit of $p_{\mathrm{surf}}(CH_4) = 10$ nbar (1σ-level) is derived from our observations. At 3σ the upper limit is 50 nbar.

In any case, these upper limits are three orders of magnitude below Pluto's atmospheric pressure, meaning that if a global atmosphere exists on Haumea it is extremely tenuous.

Ring fit to the secondary events. Apart from the occultations by the main body, the light curves reveal brief dimmings from most of the sites before and/or after the main event. The timings of these events (see Extended Data Table 2) were extracted by fitting square-well ring profiles to the short events, in the same way as for Chariklo (ref. 7). However, the only resolved profiles come from the Konkoly 1-m telescope (Fig. 1). At that station, we derive a radial width (in the ring plane) of $W_{\mathrm{ring}} \approx 74$ km at ingress and $W_{\mathrm{ring}} \approx 44$ km at egress, with respective apparent opacities (along the line of sight) of $p' = 0.55$ and $p' = 0.56$. This implies so-called equivalent widths $W_{\mathrm{equiv}} = W_{\mathrm{ring}} p'$ of 41 km and 25 km, respectively, a measure of the radially integrated amount of material contained in the ring. Note that the apparent opacity is related to the apparent optical depth through $\tau' = -\ln(1 - p')$. Converting the apparent optical depth into a ring-normal optical depth τ_N is not straightforward, because the conversion depends on whether the ring is mono- or polylayer (and it can be neither, as these are idealized cases); it is complicated further by diffraction by individual ring particles[7].

For the rest of the sites, the ring profiles are not resolved and large readout times between integration intervals prevent a full recording of each event. Consequently, we used a simple model with a uniform ring of width of 70 km and apparent opacity of 0.5 that provides the typical average equivalent width observed at Konkoly. These fits account for the readout times between exposures and eventually provide the timings of the synthetic events. Note that in one case (Skalnate egress; Fig. 1) the ring is not detected because it should occur during a readout time. Note also that at several stations (Lajatico, San Marcello Pistoiese, Asiago and Wendelstein) the egress ring event is not recorded, not as a result of a lack of signal-to-noise ratio, but because our view of the ring is blocked by Haumea's body (Fig. 3).

The locations of the twelve secondary events, projected in the sky plane, enables the retrieval of the full ring orbit, assuming an apparent elliptical shape and using the same approach as for Haumea's limb fitting, that is, five adjusted parameters for the ring model. The fit returns a χ^2 per degree of freedom of $\chi^2_{\mathrm{pdf}} = 0.43$, indicating a satisfactory fit. The radial standard deviation is 27 km, which indicates the typical quality of our fit in a more physical unit. The resulting ring model, in which we also outline the assumed physical width of 70 km, is displayed in Fig. 3; Extended Data Fig. 4 shows an expanded view of the northern part of the ring for a better view.

The parameters of the elliptical fit are $a'_{\mathrm{ring}} = 2,287^{+75}_{-45}$ km for the apparent semi-major axis of the ellipse, and $b'_{\mathrm{ring}} = 541 \pm 23$ km for the semi-minor axis. The position angle of the minor axis is $P_{\mathrm{ring}} = -74.3° \pm 1.3°$. Assuming a circular ring, this implies a ring radius of $r_{\mathrm{ring}} = 2,287^{+75}_{-45}$ km and an opening angle of $B_{\mathrm{ring}} = \arcsin(b'/a') = 13.8° \pm 0.5°$. The circular ring assumption is supported by the fact that the centre of the fitted ellipse of the ring and the fitted centre of Haumea's limb coincide to within the error bars (Fig. 3). Moreover, the position angle $P_{\mathrm{ring}} = -74.3° \pm 1.3°$ also coincides with that of the minor axis of the limb, $P_{\mathrm{limb}} = -76.3° \pm 1.2°$. This is further strong evidence that we are observing a ring that has settled into Haumea's equatorial plane.

The radius of the ring falls where the 3:1 spin–orbit resonance is expected. That second-order resonance occurs when $2\kappa = \omega - n$, where κ is the horizontal epicyclic frequency of a particle, n is its mean motion and ω is Haumea's spin rate. The frequencies κ and n are classically given by $n^2 = (\mathrm{d}U_0/\mathrm{d}r)/r$ and $\kappa^2 = \mathrm{d}(r^4 n^2)/r^3$, where $U_0(r)$ is the azimuthally averaged gravitational potential of the primary at distance r from the centre. Assuming a homogeneous ellipsoid with semi-axes $a > b > c$ and defining its oblateness as $f = \left[\sqrt{(a^2 + b^2)/2} - c\right]/a$, then to lowest-order in f we obtain $U_0(r) \approx -(GM/r)[1 + (f/5)(a/r)^2]$, where G is the gravitational constant and M is Haumea's mass. Using the values of a, b and c derived below and $M = (4.006 \pm 0.040) \times 10^{21}$ kg (ref. 20), we find that the 3:1 resonance occurs at $r_{3:1} = 2,285 \pm 8$ km, coincident with the ring radius to within error bars.

Constraints on the ring brightness from photometric observations. We modelled the brightness of Haumea and its ring as in refs 8, 33 and 34 to estimate the evolution of the absolute magnitude of the Haumea system as a function of epoch (given that we know the orientation of the ring, the shape of the main body, the geometric albedo of the main body and the radius of the ring, and leaving as a free parameter the ring reflectivity I/F, and assuming a width of 70 km for the ring; see previous section). In Extended Data Fig. 5 we plot the absolute magnitude as a function of epoch.

To compare the predictions with old observations we used the earliest available magnitude reported to the minor planet centre database (for 1955), which was based on Digitized Sky Survey (DSS) images of Haumea.The reported value is 16.4 mag in the R band (http://www.minorplanetcenter.net/db_search/show_object?utf8=%E2%9C%93&object_id=Haumea). This can be translated into V magnitude by using the $V - R$ colour of Haumea[35], which is 0.33 ± 0.01. Hence, the derived V magnitude is 16.77, which we corrected for phase angle (using the 0.11 mag per degree slope parameter for Haumea[15]) and for heliocentric and geocentric distances to determine an absolute magnitude $H_V = -0.266$ mag for 1955 with an estimated uncertainty of 20%, not including the rotational variability. For 1991 and 1994 we used the DSS data reported to the minor planet centre database, which we assume can have a photometric uncertainty of at least around 20%. We provided a new data point in 2017 by observing Haumea on several nights using the 1.5-m telescope at Sierra Nevada observatory. The standard V and R Johnson Cousins filters were used and Landolt reference stars were observed. This was done in several photometric nights so that an absolute calibration could be performed with good accuracy. The magnitudes were corrected for geocentric and heliocentric distances as well as for the phase-angle effect using the same coefficient mentioned above. The rotational phase at the time of the observations was accounted for to derive the rotationally averaged absolute magnitude, $H_V = +0.35 \pm 0.06$.

The results are plotted in Extended Data Fig. 5. To explain the bright absolute magnitude of Haumea in 1955, a ring system with a considerable brightness contribution would seem necessary, but such a ring system would result in too steep behaviour that cannot explain the much better data in 2005 and 2017. Hence we discard it. Our current best guess is $I/F \approx 0.09$ for a 70-km-wide ring. This is comparable to the reflectivity of Chariklo's main ring[7], while being brighter than the similar Uranian rings[36] α and β ($I/F \approx 0.05$), and dimmer than Saturn's A ring[37] ($I/F \approx 0.5$), all features that have opacities comparable to Haumea's ring. This number should be taken with care, however, as other values of W_{ring} are possible and would provide updated values satisfying $W_{\mathrm{ring}} \times I/F \approx 7$ km. Also, considering the large uncertainties in the oldest data, it is clear that more data would be needed to better constrain our model. The photometric observations give support to the pole orientation with J2000 equatorial coordinates of (285.1°, −10.6°) rather than (312.3°, −18.6°), because the latter gives a model that is completely out of phase compared to the observations. In particular, such a model would require an increase in the absolute magnitude from 2005 to 2017, which we can disregard. The ring that best fits the photometry data in 2005 and 2017 contributes about 2.5% of the total flux of the system in 2017.

We followed the approaches in refs 8 and 34 to determine the variation in the amplitude of the rotational light curve with epoch, including a constant contribution from the satellite Hi'iaka. We could reproduce the reported[1,17] amplitudes of the rotational variability in 2005 and 2007 and our own data in 2017 by using a triaxial body with $a = 1{,}161$ km, $b = 852$ km and $c = 513$ km (see Methods section 'Three-dimensional shape and density of Haumea'). The ring cannot contribute more than 5% of the flux because in that case the rate of change of the amplitude is too steep to be compatible with the observations (Extended Data Fig. 5b). In addition, the pole solution (312.3°, −18.6°) can be discarded as it produces a model that is out of phase compared to the observations of the amplitude of the light curve.

Regarding the origin of the ring, different mechanisms are possible. Impacts on Haumea might launch material in orbit around it, with some material ending up as a ring inside the Roche limit, possibly concentrated in particularly stable regions such as a spin–orbit resonance or near a shepherding satellite. Alternatively, the tidal disruption or collisional disruption of a previously existing satellite could generate a debris disk that would then stay in orbit. Several possible mechanisms of ring formation have been discussed for the ring systems found around Chariklo[7,38–40] and Chiron[8], some of which could also apply to Haumea. Other scenarios that invoke cometary activity as the source of rings[41] do not apply to Haumea because such activity is unplausible for a remote and large TNO. In any case, the ring formation process is probably related to that which formed Hi'iaka and Namaka, and perhaps the orbitally related Haumea family[42].

Some models[43] include the possibility that rings can be found only between 8 AU and 20 AU from the Sun. This is in principle ruled out by the detection of Haumea's ring, currently situated at a heliocentric distance of more than 50 AU, although it cannot be disregarded that Haumea could have formed much closer in and migrated to its current position with the ring already formed.

Geometric albedo of Haumea. If the projected size of a Solar System body (A) and its brightness are known, we can determine the geometric albedo by using

$$p_v = \frac{10^{0.4(V_{\rm Sun}-H_{\rm V})}}{A/\pi}$$

where $V_{\rm Sun}$ is the magnitude of the Sun ($m_{\rm V}=-26.74$) and $H_{\rm V}$ is the instantaneous absolute magnitude, which can be obtained from the rotationally averaged absolute magnitude ($\langle H_{\rm V}\rangle$) of Haumea main body. The value of $\langle H_{\rm V}\rangle$ determined from the ground includes the contribution of the ring and the satellites Hi'iaka and Namaka, which should be discounted if we want to compute the true geometric albedo of the main body using the effective diameter or projected area of the occultation. The value of $\langle H_{\rm V}\rangle$ of the Haumea system determined from ground-based observations[15] is 0.428 ± 0.011 mag. However, this absolute magnitude corresponds to 2005 and we should use the value derived in 2017, plotted in Extended Data Fig. 5, which is brighter by 0.07 mag. The brightness contribution of the ring to the total brightness of the Haumea system (main body + ring) was assessed to be almost negligible in the previous section. Hence, if we subtract a contribution of 2.5% from the brightness to the $\langle H_{\rm V}\rangle$ measurements of the Haumea system and an approximately 11% contribution from Hi'iaka[20,44] and Namaka, then the correct $H_{\rm V}$ value for Haumea's main body at the time of the occultation becomes $0.35 + 0.14 + 0.32/2$ (we had to add at least 0.32/2 mag because Haumea was at its rotational minimum at the time of the occultation, as explained in Methods section 'Three-dimensional shape and density of Haumea'). The resulting geometric albedo, inserting the area A from the occultation, would be 0.51, which is much smaller than the most recently determined value of $0.804^{+0.062}_{-0.095}$, derived on the basis of Herschel thermal measurements combined with Spitzer data[11]. Previous modelling of Herschel and Spitzer measurements[16] resulted in an albedo of 0.7–0.75, still much higher than the value from the occultation. The main reason for the difference comes from the fact that the occultation results give rise to a larger body than estimated previously, possibly as a result of different beaming parameters or phase integrals, or deficiencies in the modified thermal models when applied to very elongated TNOs such as Haumea. Thermal models for spherical bodies systematically underestimate the diameters and overestimate the albedos of low-obliquity ellipsoidal asteroids[45]. This seems also applicable to TNOs. In addition, the presence of the ring was not anticipated and was not taken into account in the thermal modelling. Hence, Haumea is considerably larger and less reflective than thought previously. Its surface may therefore contain a larger fraction of rock compared ice than estimated previously. With this value of the geometric albedo, reanalysis of the spectra of Haumea implies that the non-icy fraction of the surface can be much larger than the 8% proposed previously[46] when a high geometric albedo was used.

Three-dimensional shape and density of Haumea. Using the measurements of the rotational light curve performed before and after the occultation and given that we know Haumea's rotation period (3.915341 ± 0.000005 h) with a very small uncertainty[16], we can accurately determine the rotational phase at the time of the occultation. It turns out that Haumea was at its absolute brightness minimum, which means that the projected area of the body was at its minimum. This is depicted in Extended Data Fig. 6.

Because we know the amplitude of the rotational light curve (0.32 mag; ref. 10), we can use the expression that relates the amplitude of the rotational light curve of a triaxial body[19] to derive the three axes of the body:

$$\Delta m = -2.5\log\left[\frac{b}{a}\left(\frac{a^2\cos^2(\theta)+c^2\sin^2(\theta)}{b^2\cos^2(\theta)+c^2\sin^2(\theta)}\right)^{1/2}\right]$$

where $a > b > c$ are the semi-axes of the ellipsoid, Δm is the amplitude of the light curve (0.32 ± 0.006 mag) and θ is the aspect angle, which is the complementary angle to the planetocentric latitude of the sub-Earth point (assumed to be equal to the ring opening angle, as discussed earlier). This aspect angle is thus $\theta_{17} = 90° - 13.8° = 76.2° \pm 0.5°$ during the occultation in 2017, but $\theta_{09} = 90° - 6.5° = 83.5° \pm 0.5°$ in 2009, when the Hubble Space Telescope observations[10] were made, using the pole position of the ring given before. We use the amplitude from ref. 10 because it was determined from Hubble Space Telescope images that could resolve Haumea, Hi'iaka and Namaka, so the contribution of the satellites does not affect the photometry, contrary to the case of the ground-based observations.

Moreover, using the fact that the the a axis was turned to us during the occultation, we can relate the apparent semi-minor axis in 2017 ($b' = 569$ km) to the true semi-minor axis through $(b')^2 = c^2\sin^2(\theta_{17}) + a^2\cos^2(\theta_{17})$. Combining this equation with the previous one, and using the numerical values mentioned before, we obtain $a \times b \times c = (1{,}161 \pm 30)$ km $\times$ (852 ± 2) km $\times$ (513 ± 16) km. The formal error on a comes mainly from the uncertainty on Δm. The value quoted above (± 0.006) seems too optimistic to represent the oscillation due entirely to shape, so we used a more plausible value of ± 0.02 due to the possible presence of albedo features on Haumea. The formal error on b comes mainly from the limb fitting (Fig. 3), because the a axis was directed to us during the occultation. Finally, the formal error on c stems directly from the uncertainty on the apparent semi-minor axis, 569 ± 13 km, which again relies on the limb fitting.

In fact, 0.32 mag is a lower limit for Δm because the constant contribution of the ring brightness was not accounted for. The actual amplitude of the oscillation that would be caused by Haumea alone, without ring, would be larger than 0.32 mag. However, the ring contribution is small, as explained in previous sections, and the difference in the amplitude of the light curve arising from this is expected to be small. Nevertheless, we cannot neglect the possibility that unknown satellites or additional rings could also contribute a few per cent.

The density of Haumea, using the values of a, b and c derived above and the mass determination from the orbital period of Hi'iaka[20], is $1{,}885 \pm 80$ kg m^{-3}. For an a semi-axis larger than the nominal 1,161 km determined here, the density will be even less than 1,885 kg m^{-3}. For a ring brightness of 5% (which is larger than needed to fit the absolute magnitude data), the longest axis would be 2,520 km, the volume-equivalent diameter becomes 1,632 km and the density would be 1,757 kg m^{-3}. We consider this value a lower limit. Values of 1,885–1,757 kg m^{-3} are far closer to the density of the rest of the known large TNOs and are in agreement with the trend of increasing density with size (see, for example, the supplementary information in ref. 5, and refs 21 and 22).

These values can be compared to the limits imposed by the hydrostatic equilibrium of a Jacobi ellipsoid[23]. In this case, the rotational parameter $\omega^2/(\pi G\rho)$ must be bounded by 0.284 and 0.374 (ω being the spin frequency of the body, G the gravitational constant and ρ the density). Using a rotation period of 3.915341 h for Haumea, we obtain the condition $2{,}530\ {\rm kg\ m^{-3}} < \rho < 3{,}340\ {\rm kg\ m^{-3}}$. This is far from our upper limit of $1{,}885 + 80\ {\rm kg\ m^{-3}} = 1{,}965\ {\rm kg\ m^{-3}}$, showing that Haumea cannot be a homogeneous ellipsoid in hydrostatic equilibrium.

The axis ratios $b/a \approx 0.73$ and $c/a \approx 0.44$ are consistent with those of a Jacobi ellipsoid with $\omega^2/(\pi G\rho) \approx 0.35$, but the density required by that solution (2,700 kg m^{-3}) is not consistent with our measurement. It has previously been noted[24] that Haumea's shape might not be that of a fluid equilibrium Jacobi body if granular physics is used to model the shape instead of using the simple assumption of fluid behaviour. It was also concluded[24] that the density of Haumea could be much smaller than the minimum of 2,600 kg m^{-3} reported in the literature[1,10,16]. For an ellipsoidal body with $b = (a + c)/2$, we can determine an angle of friction of between 10° and 15° from figure 4 of ref. 25 for a density of 1,885 kg m^{-3}. A non-homogeneous body can also depart from the classical equilibrium shapes. Differentiation can be expected in large bodies such as Haumea, but it remains to be seen whether feasible mass concentrations towards the nucleus can explain its current shape and density.

Analysis of the Crni Vrh images. Given that the images were acquired while the telescope was guided at a sidereal rate and moving at a speed of 40 arcsec per minute in the north–south direction, with 300-s integrations, the resulting images show trailed stars. By using 300 s of exposure time and reading out the CCD in 15 s, the percentage of 'deadtime' was only around 5%. This comes at the expense of increasing the background noise considerably. The images were dark-subtracted and flatfielded following standard procedures. To analyse the trail of the occultation star plus Haumea (both blended in a single trail), we took line profiles along the centre (and most intense) part of the trail in the different images. Given the known drift of the telescope, we can translate the pixel along the profile to time after the integration. The pixel scale was 1.4 arcsec per pixel. Plots of these line profiles are shown in Extended Data Fig. 7 for images before and during the main occultation event.

The smoothed line profile of the trail in the image at the time of the occultation shows a clear drop in intensity at an approximate time indicated by the dashed vertical line in Extended Data Fig. 7. This corresponds to the time when the star disappeared as a result of the occultation. The intensity remains low for the rest of the integration, which means that the star did not reappear while the image was being taken. We can thus determine a disappearance time and estimate that the reappearance probably took place while the CCD camera was being readout. In addition, from the elliptical fit to the occultation chords of the rest of the sites, the reappearance time at Crni Vrh is expected to have happened approximately at the time of the readout. The timings derived in this way are shown in Table 1. Even though the time uncertainties are large and difficult to estimate, the data still provide valid information.

Data and code availability. All relevant data are available from the corresponding author on request. We have opted not to make our codes available as we cannot guarantee their correct performance on different computing platforms.

27. Desmars, J. *et al.* Orbit determination of trans-Neptunian objects and Centaurs for the prediction of stellar occultations. *Astron. Astrophys.* **584,** A96 (2015).
28. Ortiz, J. L. *et al.* A mid-term astrometric and photometric study of trans-Neptunian object (90482) Orcus. *Astron. Astrophys.* **525,** A31 (2011).
29. Altmann, M., Roeser, S., Demleitner, M., Bastian, U. & Schilbach, E. Hot Stuff for One Year (HSOY). A 583 million star proper motion catalogue derived from Gaia DR1 and PPMXL. *Astron. Astrophys.* **600,** L4 (2017).
30. Lomb, N. R. Least-squares frequency analysis of unequally spaced data. *Astrophys. Space Sci.* **39,** 447–462 (1976).
31. Dumas, C., Carry, B., & Hestroffer, D. & Merlin, F. High-contrast observations of (136108) Haumea. A crystalline water-ice multiple system. *Astron. Astrophys.* **528,** A105 (2011).
32. Benedetti-Rossi, G. *et al.* Results from the 2014 November 15th multi-chord stellar occultation by the TNO (229762) 2007 UK126. *Astron. J.* **152,** 156 (2016).
33. Duffard, R. *et al.* Photometric and spectroscopic evidence for a dense ring system around Centaur Chariklo. *Astron. Astrophys.* **568,** A79 (2014).
34. Fernández-Valenzuela, E., Ortiz, J. L., Duffard, R., Morales, N. & Santos-Sanz, P. Physical properties of Centaur (54598) Bienor from photometry. *Mon. Not. R. Astron. Soc.* **466,** 4147–4158 (2017).
35. Snodgrass, C., Carry, B., Dumas, C. & Hainaut, O. Characterisation of candidate members of (136108) Haumea's family. *Astron. Astrophys.* **511,** A72 (2010).
36. Karkoschka, E. Comprehensive photometry of the rings and 16 satellites of Uranus with the Hubble Space Telescope. *Icarus* **151,** 51–68 (2001).
37. French, R. G. *et al.* Saturn's rings at true opposition. *Publ. Astron. Soc. Pacif.* **119,** 623–642 (2007).
38. Hyodo, R. *et al.* Formation of Centaurs' rings through their partial tidal disruption during planetary encounters. *Astrophys. J.* **828,** L8 (2016).
39. Melita, M. D., Duffard, R., Ortiz, J. L. & Campo-Bagatin, A. Assessment of different formation scenarios for the ring system of (10199) Chariklo. *Astron. Astrophys.* **602,** A27 (2017).
40. Charnoz, S., Canup, R. M., Crida, A. & Dones, L. The origin of planetary ring systems. Preprint at https://arxiv.org/abs/1703.09741 (2017).
41. Pan, M. & Wu, Y. On the mass and origin of Chariklo's rings. *Astrophys. J.* **821,** 18 (2016).
42. Schlichting, H. E. & Sari, R. The creation of Haumea's collisional family. *Astrophys. J.* **700,** 1242–1246 (2009).
43. Hedman, M. M. Why are dense planetary rings only found between 8 and 20 AU? *Astrophys. J.* **801,** L33 (2015).
44. Hastings, D. M. *et al.* The short rotation period of Hi'iaka, Haumea's largest satellite. *Astron. J.* **152,** 195 (2016).
45. Hamilton Brown, R. Ellipsoidal geometry in asteroid thermal models: the standard radiometric model. *Icarus* **64,** 53–63 (1985).
46. Pinilla-Alonso, N. *et al.* The surface of (136108) Haumea (2003 EL61), the largest carbon depleted object in the trans-neptunian belt. *Astron. Astrophys.* **496,** 547–556 (2009).

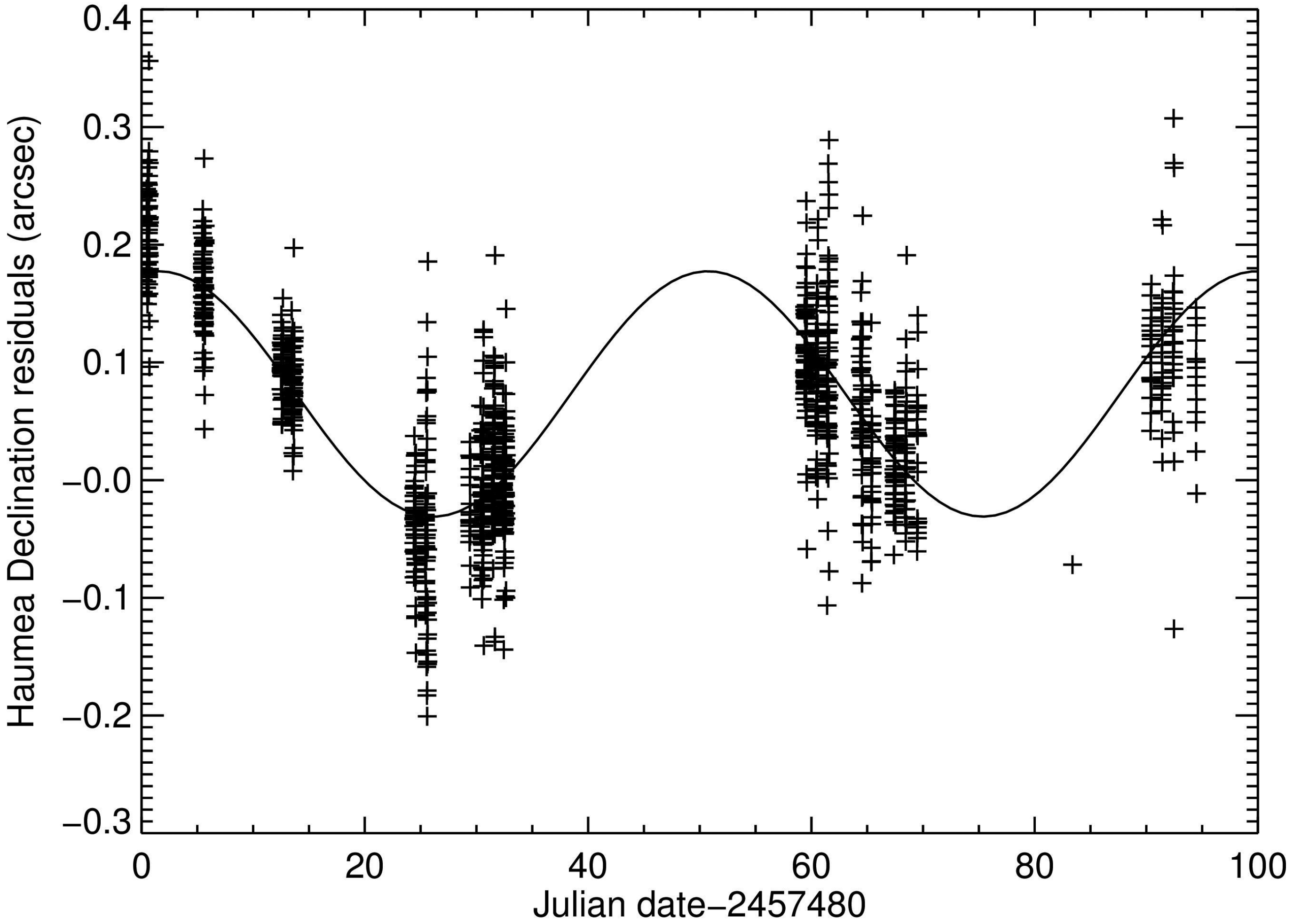

Extended Data Figure 1 | Declination residuals of Haumea astrometry. The plus symbols show the declination residuals of the observed position of the photocentre of Haumea's system with respect to the theoretical position in declination, from JPL#81 ephemerides. The residuals are shown versus the date of observation. All of the observations were obtained with the La Hita 0.77-m telescope, as explained in Methods. The thin solid line represents a sinusoidal fit to the residuals, with the period determined from a periodogram analysis that is coincident with the orbital period of the moon Hi'iaka. Outlier values have not been removed. In right ascension we did not detect an oscillating behaviour of the residuals because the orbit Hi'iaka does not extend as much as in declination and the quality of the data was not good enough to show the periodicity.

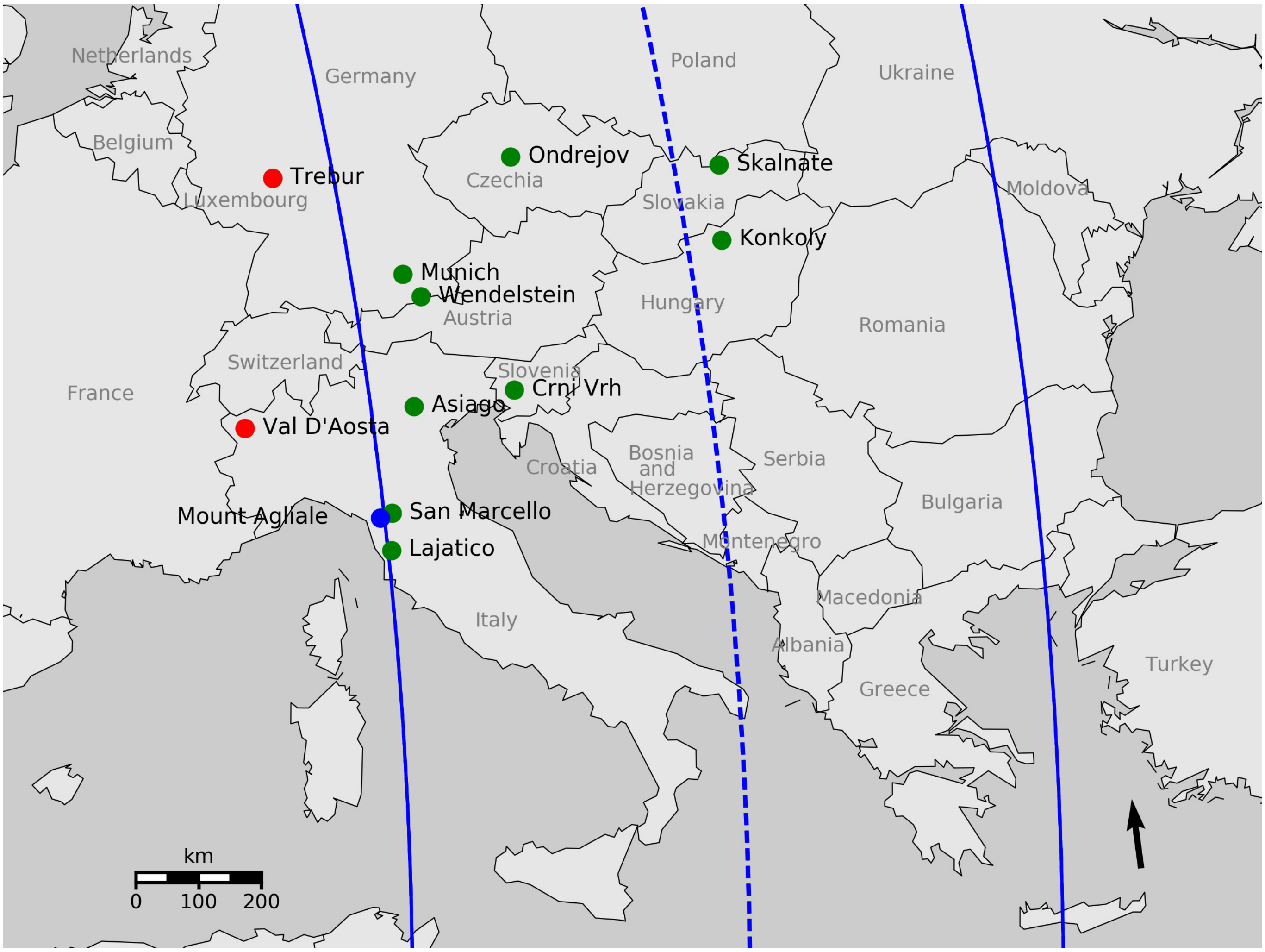

Extended Data Figure 2 | Map of Earth showing the locations of the observatories that recorded the occultation (green dots). The solid lines mark the limits of the shadow path. Mount Agliale is indicated in blue because the occultation by the main body was not positive there, but the occultation by the ring was detected. The dashed line denotes the centre of the shadow path. Note that Munich corresponds to the location of the Bavarian Public Observatory. The complete names of the observatories can be found in Table 1. The red marks at Trebur and Valle D'Aosta observatories indicate the two closest sites to the shadow path that recorded a negative occultation. The coordinates of Trebur observatory are 49° 55′ 31.5″ N, 8° 24′ 40.6″ E and the coordinates of Valle D'Aosta observatory are 45° 47′ 22″ N and 7° 28′ 42″ E. The shadow motion is from the bottom to the top of the figure.

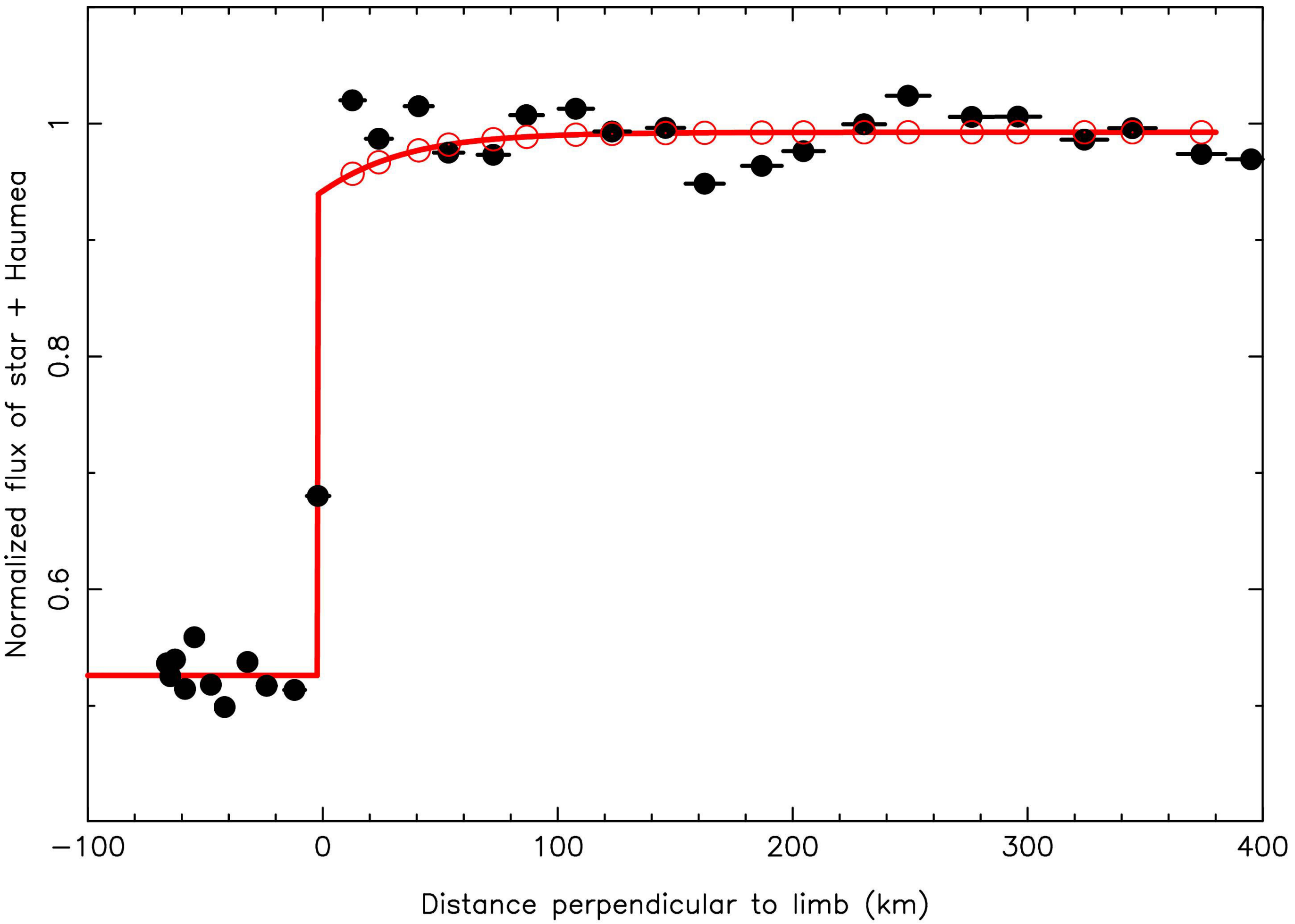

Extended Data Figure 3 | Upper limit on Haumea's N_2 atmosphere. The black filled circles show the normalized flux from the star plus Haumea, as observed from the Asiago station, which is the one that provided the highest signal-to-noise ratio and enough time resolution to look for a faint atmosphere. They combine ingress and egress data and are plotted against the distance perpendicular to the local Haumea limb, as given by the solution shown in Fig. 2. The horizontal bars associated with each data point indicate the distance interval corresponding to the integration times of each point. The red line shows an example light curve obtained with an isothermal N_2 atmosphere at $T = 40$ K and with surface pressure $p_{\mathrm{surf}} = 15$ nbar (at 3σ-level upper limit for better illustration, because the 1σ-level of 3 nbar would be difficult to notice). The red open circles show the expected flux at each data point after convolution with the finite integration point.

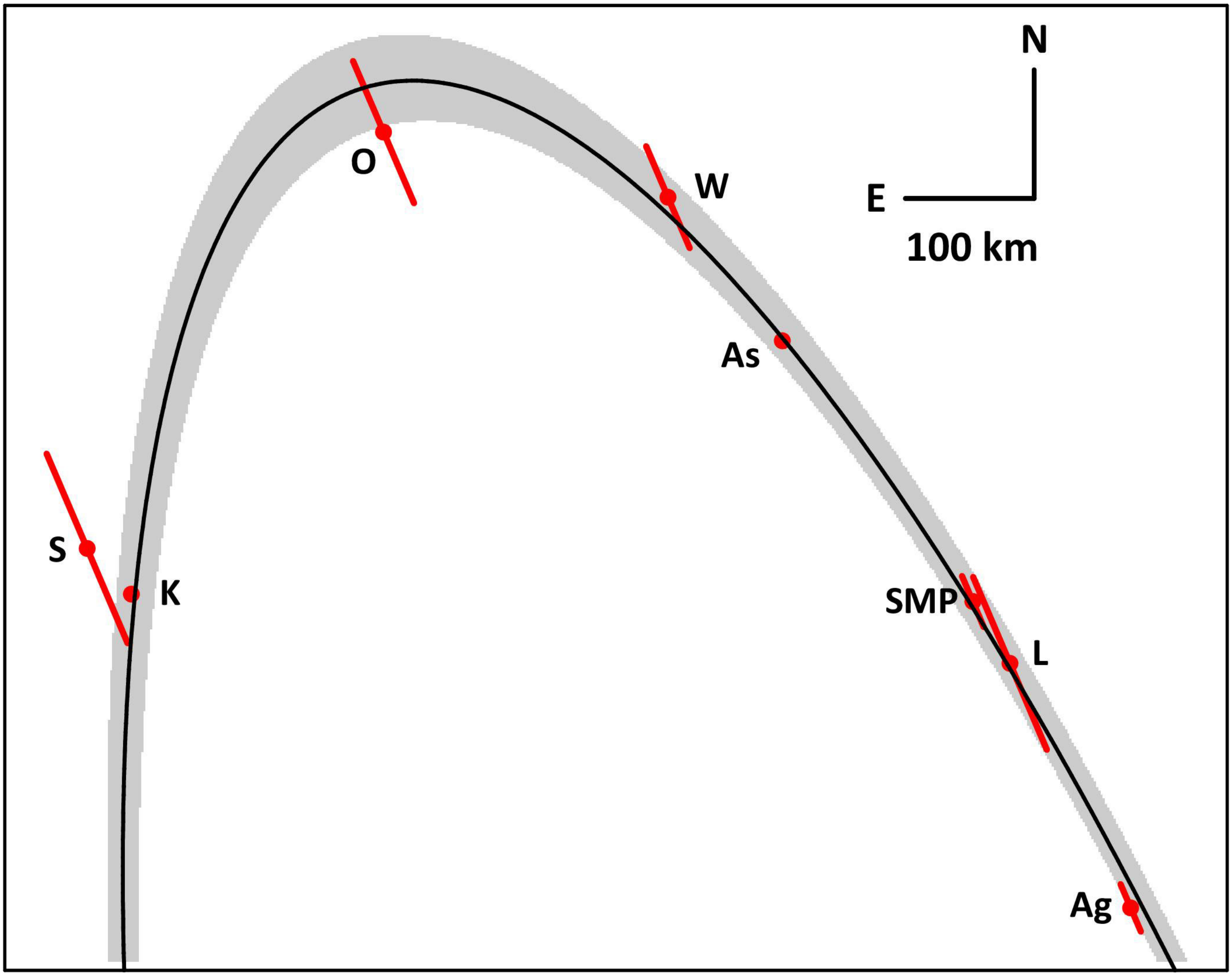

Extended Data Figure 4 | Upper part of the ring. An expanded view of Fig. 3 showing in more detail the events along the upper part of the ring. The best fitting mean ring radius $a'_{\mathrm{ring}} = 2,287^{+75}_{-45}$ km is drawn as a solid curve. The grey area shows the full extension of a semi-transparent 70-km-wide ring that is consistent with the twelve secondary events shown in Fig. 3. The lengths of the red segments indicate the uncertainties stemming from the error bars on the ring timings.

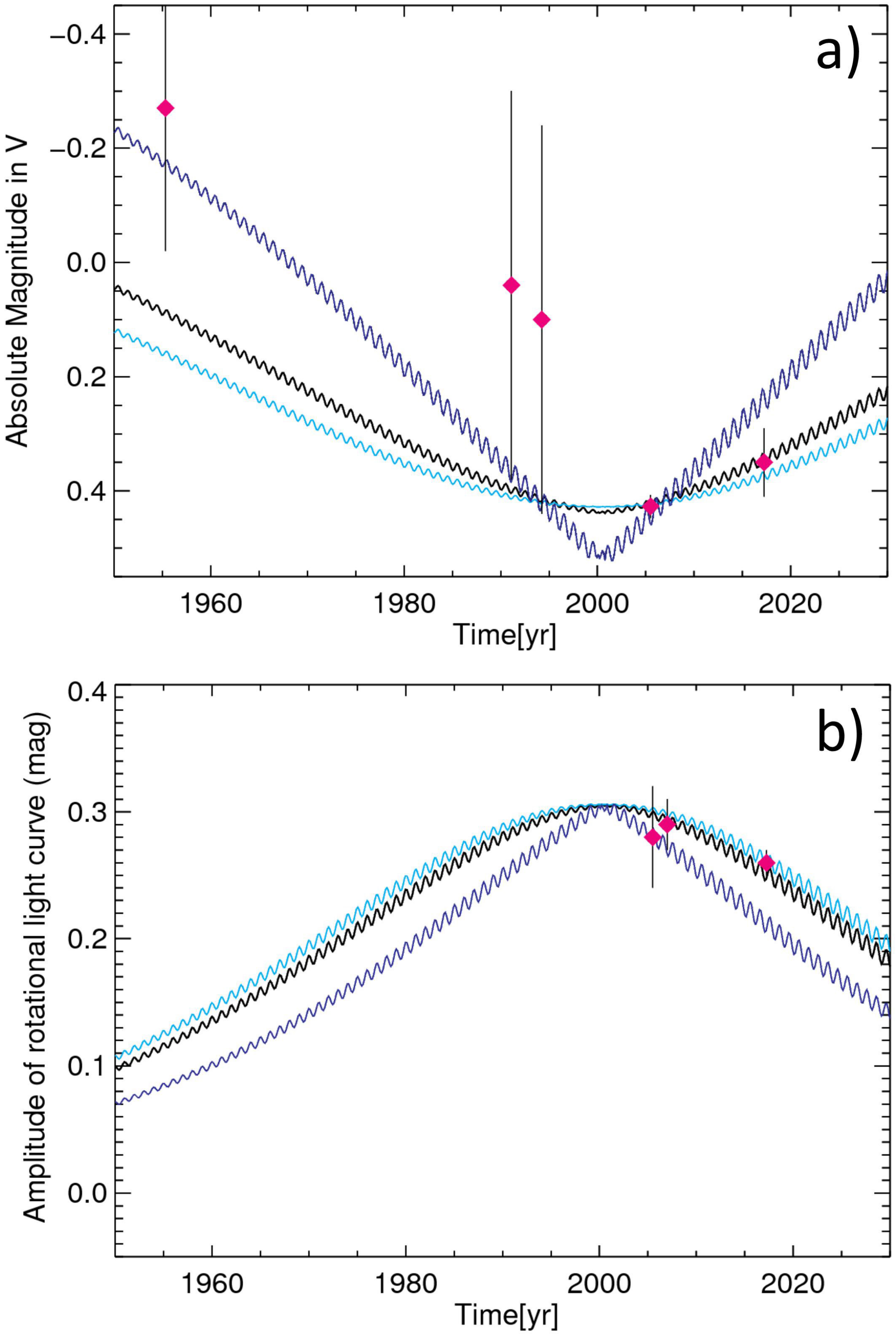

Extended Data Figure 5 | Photometric models. **a**, Absolute V-band magnitude of the Haumea system as a function of time. Diamonds represent observations and lines are models. The cyan curve represents a model without a ring, the black curve is a model with a 70-km-wide ring and with a reflectivity of $I/F = 0.09$, similar to that of Chariklo's main ring. The ring in this model contributes approximately 2.5% of the total flux of Haumea plus Hi'iaka in 2017. The dark blue curve corresponds to a model with a wider (140 km) and brighter ($I/F = 0.36$) ring, which contributes 20% of the total brightness in 2017. This model can be discarded because it would produce a change in the amplitude of the light curve that is too rapid to be compatible with the observations (see **b**). **b**, Amplitude of the rotational light curve determined from the ground for the same three models as in **a** (using the same colour coding). The diamonds represent observations from the literature[1,17] and from this work (for 2017). See Methods for further explanations. Error bars show the errors of the measurements from refs 1 and 17 and from the determination in 2017 from this work, shown in Extended Data Fig. 6.

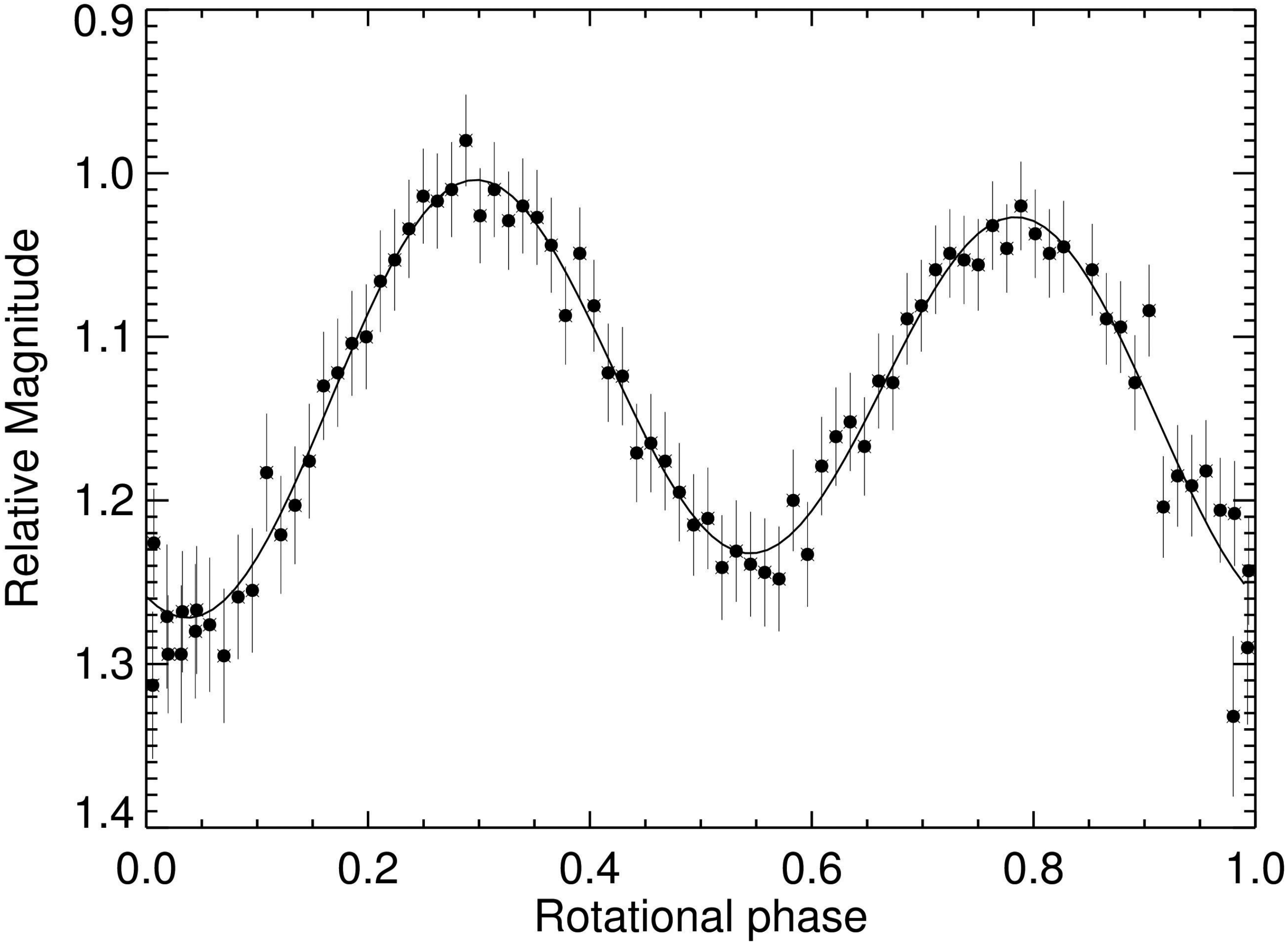

Extended Data Figure 6 | Rotational light curve of Haumea. The relative magnitude versus rotational phase obtained two days after the occultation with the Valle D'Aosta 0.81-m telescope with no filters is shown. The rotational zero phase was established at the time of the occultation and the rotation period used was 3.915341 h. Superimposed is a fit to the observational data. As can be seen, the absolute maximum in magnitude (absolute brightness minimum) is reached at the time of the occultation (arbitrarily located at a phase of 0 here), which means that the projected area of Haumea was also at its minimum. The continuous line is a fit to the data. The peak-to-peak amplitude of the light curve is 0.25 ± 0.02 mag. Error bars are 1σ.

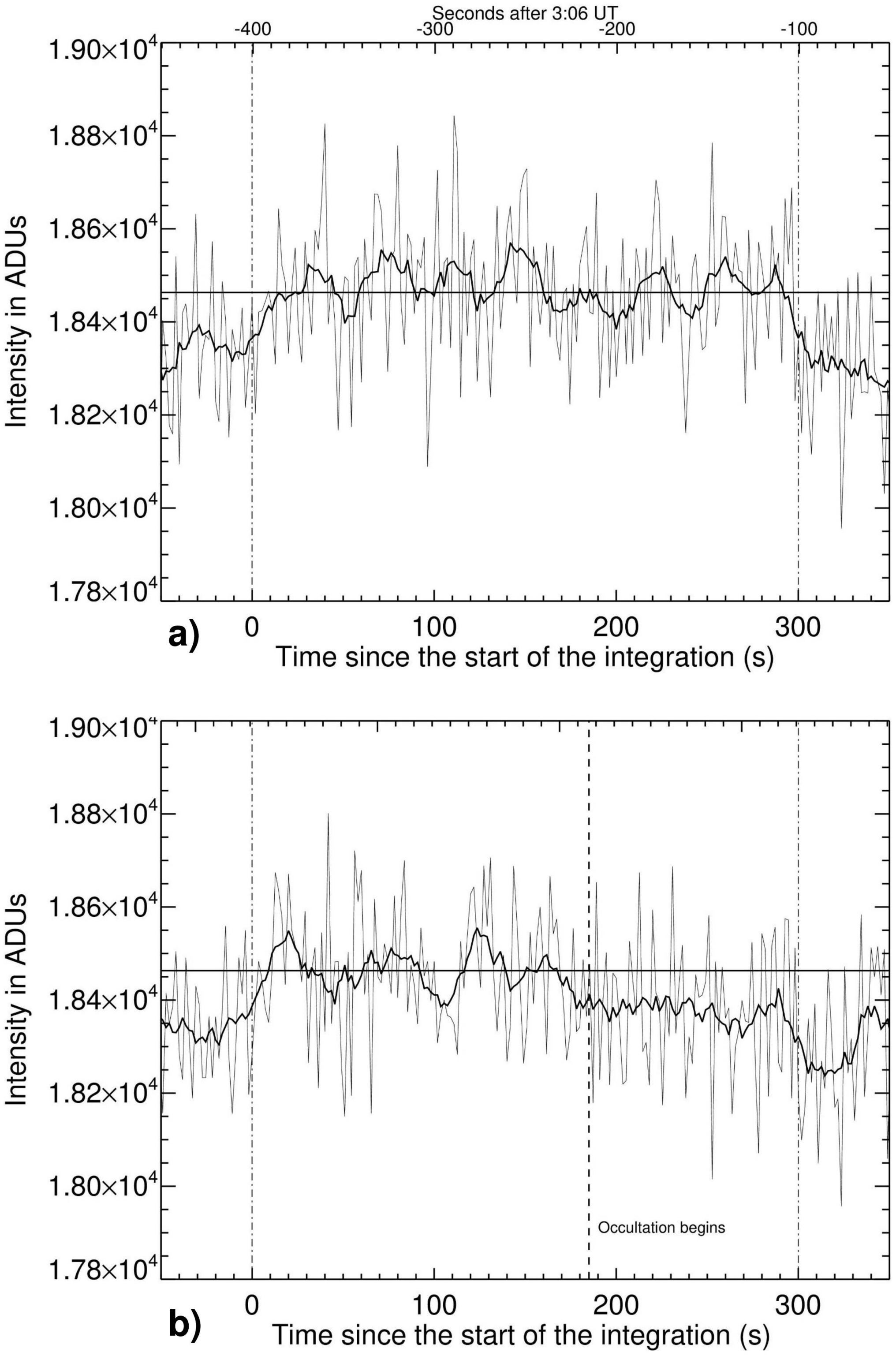

Extended Data Figure 7 | Profiles of the trails of the occultation star in two images. a, Profile along a central line in the trail of the occultation star (blended with Haumea) in a drifted image taken from Crni Vrh observatory before the main occultation. On the *y* axis we show the light intensity along the line. The line starts 40 pixels before the beginning of the trail and ends 40 pixels after the end of the trail to show the background level and that the transition from trail to background is not easy to identify. The horizontal line marks the mean intensity of the trail. The thick line represents a profile smoothed with a 10-pixel boxcar to filter the high-frequency noise. The *x* axis has been translated from pixels to time using the drift speed of 40 arcsec per minute, given the known pixel scale of the telescope. The vertical dashed-dotted lines at 0 s and 300 s mark the start and end of the integration, respectively. The UT at start of exposure was 02:59:19.50. The intensity is basically constant with time. Before 0 s and after 300 s, the line profiles decay to the background level of the image because the pixels there were outside the trail. Hence, before 0 s and after 300 s, the plot does not represent the intensity of the source but the intensity of the background. **b**, Same as **a**, but from the image at the time of the occultation. The UT at the start of the exposure was 03:04:50.11. The dashed vertical line at 185 s marks the approximate moment at which the occultation begins. The smoothed curve shows that a clear drop in the signal is produced and lasts until the end of the 300-s integration. ADU, analog-to-digital unit.

Extended Data Table 1 | Data on the occulted star

Designation	URAT1 533-182543 GaiaDR1 1233009038221203584
Magnitude[*]	B=20.88, V=17.97, R=18.000, J=15.353, H=14.791, K=14.532
Diameter[**]	~0.007 mas (~0.27 km at Haumea's distance)
Coordinates[***]	α = 14h 12m 03s.2034, δ = +16° 33' 58".642
Speed[****]	13.1 km/s

[*] From the NOMAD catalogue.

[**] Estimated from the V, B, R, J, H and K magnitudes.

[***] Coordinates in the J2000 equinox for epoch 2017.0575 from this work.

[****] Speed of Haumea with respect to the star, seen from Earth.

Extended Data Table 2 | Timing of the secondary brief occultation events from the different observing sites on 21 January 2017

Site Name and country	Coordinates Lat dd:mm:ss Lon dd:mm:ss Altitude (m)	Telescope Name Aperture Filter	Detector/Instrument Exposure (s) Cycle time (s)	Mid time of event (UTC) flux standard deviation, level of ring event detection (σ)
Skalnate Pleso Observatory -Slovakia	49°11'21.8" N 20°14'02.1" E 1826	Astelco 1300/10400 1.3 m no filter	Moravian G4-9000 10 s 15.503 s	Ingress 3:07:04.1±5.6 0.044, 2.1
Skalnate Pleso Observatory -Slovakia	49°11'21.8" N 20°14'02.1" E 1826	Astelco 1300/10400 1.3 m no filter	Moravian G4-9000 10 s 15.503 s	Egress* 3:11:50±2.4 0.044, n.a.
Konkoly Observatory -Hungary	47°55'01.6" N 19°53'41.5" E 935	RCC 1.0 m no filter	Andor iXon 888 1 s 1.007 s	Ingress 3:06:58.1±0.3 0.079, 4.5
Konkoly Observatory -Hungary	47°55'01.6" N 19°53'41.5" E 935	RCC 1.0 m no filter	Andor iXon 888 1 s 1.007 s	Egress 3:11:40.7±0.2 0.068, 3.5
Ondrejov Observatory -Czech Republic	49°54'32.6" N 14°46'53.3" E 526	Ondrejov 650/2675 0.65 m no filter	Moravian G2-3200 8 s 9.721 s	Ingress 3:06:48.4±4.2 0.041, 2.5
Ondrejov Observatory -Czech Republic	49°54'32.6" N 14°46'53.3" E 526	Ondrejov 650/2675 0.65 m no filter	Moravian G2-3200 8 s 9.721 s	Egress 3:10:51.6±3.0 0.041, 2.9
Wendelstein Observatory -Germany	47°42'13.6" N 12°00'44" E 1838	2.0m Fraunhofer f/7.8 2.0 m r'	WWFI** 10 s 14.536 s	Ingress 3:06:39.5±3.9 0.021, 4.9
Asiago observatory Cima Ekar -Italy	45°50'54.9"N 11°34'08.4"E 1376	Copernico 1.82 m f/9 1.8m no filter	AFOSC*** 2 s 5.026 s	Ingress 3:06:35.4±0.3 0.029, 8.8
S. Marcello Pistoiese observatory -Italy	44°03'51.0" N 10°48'14.0" E 965	0.60 f/4 0.6m no filter	Apogee Alta U6 10 s 11.877 s	Ingress 3:06:38.8±1.5 0.039, 5.8
Lajatico Astronomical Centre -Italy	43°25'44.7" N 10°43'01.2" E 433	RC 50 cm f/9 0.5 m no filter	Moravian G3-1000 15 s 16.254 s	Ingress 3:06:37.9±5.1 0.067, 1.6
Mount Agliale observatory -Italy	43°59’43.1’’ N 10°30’53.8’’ E 758	50 cm f/4.6 0.5 m no filter	FLI proline 4710 15 s 16.724 s	Ingress 3:06:56.7±1.4 0.031, 4.5
Mount Agliale observatory -Italy	43°59’43.1’’ N 10°30’53.8’’ E 758	50 cm f/4.6 0.5 m no filter	FLI proline 4710 15 s 16.724 s	Egress 3:08:15.3±4.2 0.031, 5.4

*The egress time at Skalnate is not a real detection of the ring; see Fig. 3.

**Information on the instrument used in this observatory can be obtained from http://www.usm.uni-muenchen.de/wendelstein/htdocs/wwfi.html.

***Information on the instrument used can be obtained at http://www.pd.astro.it/index.php/en/asiago-info-eng/who-we-are/136-asiago-eng/250-afosc.html.